LETTER

doi:10.1038/nature25982

Carbonate-sensitive phytotransferrin controls high-affinity iron uptake in diatoms

Jeffrey B. McQuaid[1,2], Adam B. Kustka[3], Miroslav Oborník[4,5], Aleš Horák[4,5], John P. McCrow[1], Bogumil J. Karas[1]†, Hong Zheng[1], Theodor Kindeberg[2], Andreas J. Andersson[2], Katherine A. Barbeau[2] & Andrew E. Allen[1,2]

In vast areas of the ocean, the scarcity of iron controls the growth and productivity of phytoplankton[1,2]. Although most dissolved iron in the marine environment is complexed with organic molecules[3], picomolar amounts of labile inorganic iron species (labile iron) are maintained within the euphotic zone[4] and serve as an important source of iron for eukaryotic phytoplankton and particularly for diatoms[5]. Genome-enabled studies of labile iron utilization by diatoms have previously revealed novel iron-responsive transcripts[6,7], including the ferric iron-concentrating protein ISIP2A[8], but the mechanism behind the acquisition of picomolar labile iron remains unknown. Here we show that ISIP2A is a phytotransferrin that independently and convergently evolved carbonate ion-coordinated ferric iron binding. Deletion of *ISIP2A* disrupts high-affinity iron uptake in the diatom *Phaeodactylum tricornutum*, and uptake is restored by complementation with human transferrin. ISIP2A is internalized by endocytosis, and manipulation of the seawater carbonic acid system reveals a second-order dependence on the concentrations of labile iron and carbonate ions. In *P. tricornutum*, the synergistic interaction of labile iron and carbonate ions occurs at environmentally relevant concentrations, revealing that carbonate availability co-limits iron uptake. Phytotransferrin sequences have a broad taxonomic distribution[8] and are abundant in marine environmental genomic datasets[9,10], suggesting that acidification-driven declines in the concentration of seawater carbonate ions will have a negative effect on this globally important eukaryotic iron acquisition mechanism.

The iron cargo protein transferrin is thought to have originated in metazoa as an adaptation to multicellularity[11]. In vertebrates, serum transferrin circulates in the blood, binding labile ferric iron (Fe′) with high affinity ($K_d^{Fe'} \approx 1–10$ pM) and distributing iron to cells via receptor-mediated endocytosis[12]. Transferrin binds iron tightly by coordinating ferric iron with an exogenous carbonate anion (CO_3^{2-}). Following endocytosis, the carbonate anion is protonated and ferric iron is reduced, disrupting Fe coordination and initiating the release of iron[13]. Recent discoveries of ferric-iron-concentrating ISIP2A proteins in diatoms[7,8] and transferrin in the green alga *Dunaliella salina*[14] suggest that transferrin-like iron acquisition mechanisms are not limited to multicellular organisms. We used a marine microeukaryote transcriptional dataset to reconstruct the phylogenetic histories of ISIP2A and transferrin, revealing a common origin in phosphonate-binding periplasmic proteins (PBPs; Fig. 1). Transferrins and the ISIP2A clade of algal transferrin-like proteins (herein phytotransferrin, or pTF[15]) are functional analogues that have convergently added iron coordination sites onto an anion-binding precursor protein (Extended Data Fig. 1a). The evolution of phytotransferrin marks the third occasion in which anion-coordinated iron binding has arisen from the bacterial PBP family[16], highlighting the fundamental role coordinating anions have within the transferrin superfamily[13].

Molecular dating (by PhyloBayes) estimates the appearance of phytotransferrins to between 914 and 671 million years ago, which is consistent with the inferred changes to Neoproterozoic marine redox states[17] and the subsequent requirements to develop mechanisms to access dilute ferric iron (Extended Data Fig. 2). Transferrin and phytotransferrin are simultaneously present in the genomes of deeply branching chlorophyte algae (Extended Data Fig. 3), although our phylogenetic reconstruction suggests that these proteins were acquired through separate events. Whereas transferrin appears to have been vertically inherited from marine archaea, the chlorophyte acquisition of phytotransferrin is less clear, plausibly occurring through endosymbiotic or horizontal gene transfer. Unlike transferrins, phytotransferrins are often transmembrane anchored (Supplementary Table 2), a selective advantage for unicellular organisms that probably contributes to its wide phylogenetic distribution among marine plankton.

To examine the role of phytotransferrin in high-affinity iron uptake in diatoms, we used TALE nucleases to disrupt *ISIP2A* (hereafter *ΔISIP2A*) in *P. tricornutum* (Fig. 2a and Extended Data Fig. 4a). In artificial seawater in which the concentration of labile inorganic iron species ([Fe′]) is controlled with excess EDTA, *ΔISIP2A* has significantly reduced growth rates at low [Fe′] (Extended Data Fig. 4b). Short-term ^{59}Fe uptake rates of *ΔISIP2A* are reduced by more than 90%, confirming the role of ISIP2A in high-affinity iron uptake (Fig. 2b). In *P. tricornutum*, ISIP2A is one of three transmembrane-anchored phytotransferrin homologues (Extended Data Fig. 1b); however, *ISIP2A* dominates transcriptional abundance, accounting for 95% of all phytotransferrin transcripts[18]. Uptake of ^{59}Fe-ferrioxamine B is not affected in *ΔISIP2A*, which suggests a separate mechanism for the uptake of complexed iron (Extended Data Fig. 4c).

To determine whether ISIP2A is a functional analogue of transferrin, codon-optimized N- and C-terminal domains of human serum transferrin (hTF) were fused to the signal peptide and transmembrane anchor of *ISIP2A* and reintroduced into *ΔISIP2A* via conjugation[19]. The N-terminal domain of hTF fully restored high-affinity iron uptake equal to that of ISIP2A, whereas the C-domain partially restored uptake (Fig. 2b), confirming phytotransferrin to be a functional analogue of transferrin and suggesting that both proteins use similar iron-binding, -internalization and -release mechanisms. In hTF, mutation of the conserved tyrosine ligands disrupts iron coordination[11]. In ISIP2A, mutagenesis of the analogous tyrosines decreases short-term uptake rates by 50%, providing further evidence of a shared mechanism (Fig. 2c).

Internalization through endocytosis is required for the release of transferrin-bound iron[20]. In *P. tricornutum*, inclusion of an endocytosis inhibitor decreases short-term ^{59}Fe′ uptake (Extended Data Fig. 4d). When ISIP2A is labelled with fluorescent protein, ISIP2A–RFP localizes to the outer membrane, small internal vesicles and endosome-like

[1]J. Craig Venter Institute, Microbial and Environmental Genomics, La Jolla, California 92037, USA. [2]Scripps Institution of Oceanography, University of California, La Jolla, California 92093, USA. [3]Rutgers University–Newark, Earth and Environmental Sciences, Newark, New Jersey 07102, USA. [4]Biology Centre CAS, Institute of Parasitology, Branišovská 31, 370 05 České Budějovice, Czech Republic. [5]University of South Bohemia, Faculty of Science, Branišovská 31, 370 05 České Budějovice, Czech Republic. †Present address: Designer Microbes Inc., London, Ontario N6G4X8, Canada.

© 2018 Macmillan Publishers Limited, part of Springer Nature. All rights reserved.

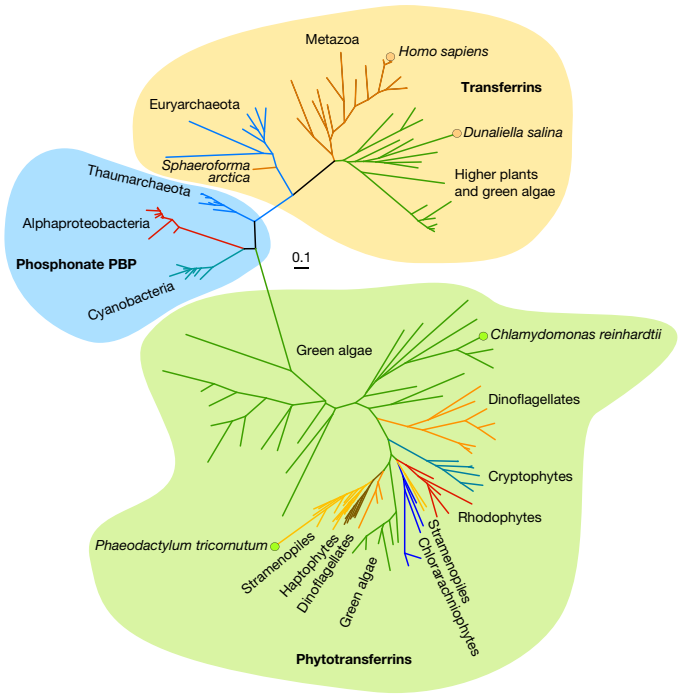

Figure 1 | Transferrin and phytotransferrin are functional analogues with a common origin. Maximum likelihood phylogenetic tree of the divergence of transferrin and phytotransferrin from ancestral PBPs as inferred from amino acid sequences. Branch colour denotes phylogenetic group, and circles at branch ends denote characterized iron-binding proteins: hTF (*H. sapiens*), triplicated transferrin (TTF1, *D. salina*), Fe-assimilation protein (FEA1, *Chlamydomonas reinhardtii*) and ISIP2A (*P. tricornutum*). Scale bar, 0.1 amino acid substitutions per position.

structures, a pattern that is consistent with internalization through endocytosis[20] (Fig. 2d). The receptor-like iron-regulated protein ISIP1[6,7] was co-visualized, however cell-surface interactions with ISIP2A were not apparent (Fig. 2d). When iron-limited *P. tricornutum* is stained with a membrane-impermeable dye and pulsed with Fe′, portions of the outer membrane are internalized (Extended Data Fig. 4e). Because endocytosis is restricted to eukaryotic organisms, phytotransferrin is a factor that probably contributes to the rapid response of diatoms and other eukaryotic plankton to iron fertilization events in high-nutrient low-chlorophyll regions[2].

In both human[12] and algal[21] transferrin, CO_3^{2-} is required for the efficient binding of iron. To investigate the role of CO_3^{2-} in phytotransferrin-mediated Fe′ uptake, we resuspended cultures of *P. tricornutum* that were acclimatized to a low-iron environment into pH-controlled ^{59}Fe-uptake medium and manipulated carbonate ion availability [CO_3^{2-}] by $NaHCO_3$ addition (Extended Data Table 1). At both low and high [Fe′], short-term Fe′ uptake rates were positively correlated with [CO_3^{2-}], consistent with a transferrin-like mechanism[12], whereas the uptake of Fe-ferrioxamine B was unaffected (Fig. 3a and Extended Data Fig. 5a). In Δ*ISIP2A*, ^{59}Fe′ uptake remained correlated with [CO_3^{2-}]; this probably reflects the activity of ISIP2A homologues (Extended Data Fig. 1b).

Iron binds to transferrin through a synergistic interaction between Fe′ and CO_3^{2-}, and neither substrate binds in the absence of the other[13]. This synergistic binding is a defining characteristic of transferrin[12], and in the above experiments the interaction between Fe′ and CO_3^{2-} is significant ($P = 2 \times 10^{-6}$), demonstrating a second-order rate dependency (Fig. 3b). Using these as representative measurements, we derived approximations for the pseudo-first-order rate constants for the dependency of Fe uptake on Fe′ (0.78 ± 0.05 mol Fe per cell per h per M Fe′ (hereafter mol Fe cell^{-1} h^{-1} (M Fe′)$^{-1}$) and CO_3^{2-} (0.0016 ± 0.0009 mol Fe per cell per h per M CO_3^{2-} (hereafter mol Fe cell^{-1} h^{-1} (M CO_3^{2-})$^{-1}$; Extended Data Fig. 6). Although organic

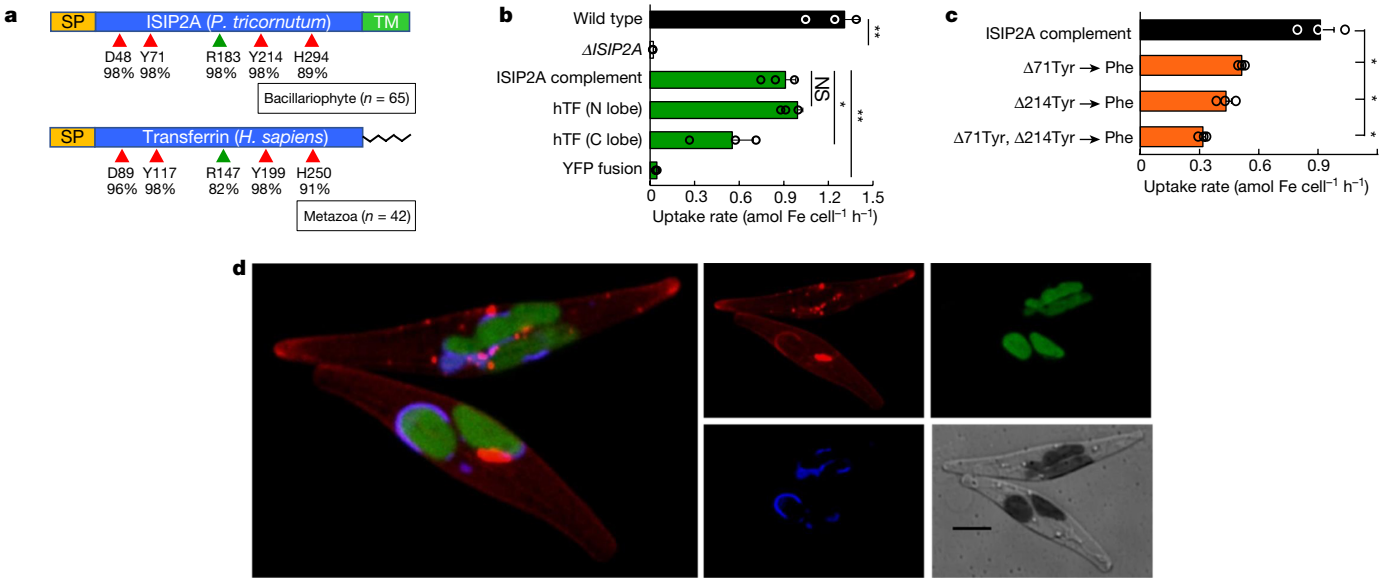

Figure 2 | Characterization of phytotransferrin ISIP2A (*P. tricornutum*). **a**, Schematic of phytotransferrin (ISIP2A) and hTF (N-terminal domain). Locations and per cent conservation of putative iron- and carbonate-coordinating amino acids (red and green triangles, respectively). SP, signal peptide; TM, transmembrane domain. **b**, High-affinity iron uptake (in attomole (amol) Fe cell^{-1} h^{-1}) is disrupted in Δ*ISIP2A* and restored in hTF- and ISIP2A-complemented cultures. YFP, yellow fluorescent protein control. **c**, Site-directed mutagenesis of putative iron-coordinating residues. **d**, In *P. tricornutum* acclimatized to low-iron concentrations, RFP-labelled ISIP2A (red) localizes to the outer membrane and internal vesicles. Iron-regulated ISIP1 (blue) and plastid (green) are co-visualized. Scale bar, 5 μm. **b**, **c**, Data are mean ± s.e.m.; $n = 3$ biological replicates; $^*P < 0.05$; $^{**}P < 0.01$; NS, not significant; paired *t*-test. **d**, Representative image of $n = 5$ biological replicates.

© 2018 Macmillan Publishers Limited, part of Springer Nature. All rights reserved.

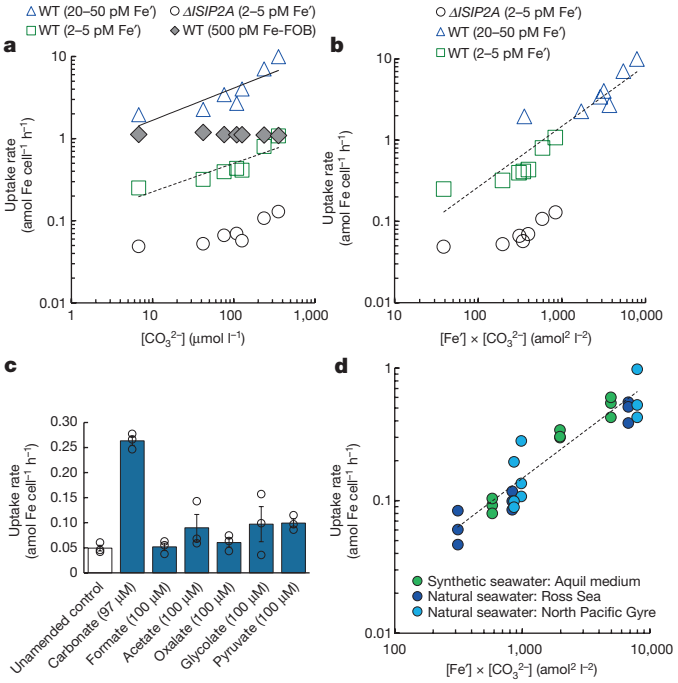

Figure 3 | The synergistic interaction of Fe′ and CO_3^{2-} determines Fe′ uptake rates. a, ^{59}Fe′ uptake rates of *P. tricornutum* resuspended in pH-controlled synthetic seawater are correlated to $[CO_3^{2-}]$, whereas the uptake of ^{59}Fe-ferrioxamine B is not positively correlated. $P = 8 \times 10^{-5}$ (solid line), $P = 3 \times 10^{-5}$ (dashed) on $n = 7$ individual experiments per regression. WT, wild type. **b**, Data from **a** replotted as a function of $[Fe'] \times [CO_3^{2-}]$, revealing a synergistic interaction. Linear regression $P = 9 \times 10^{-10}$, $n = 14$ individual experiments. **c**, ^{59}Fe′ uptake rates are not restored with organic acids, suggesting an *in vivo* specificity for carbonate. Data are mean ± s.e.m.; $n = 3$ biological replicates; $^{**}P < 0.01$, all others $P > 0.05$; paired *t*-test. **d**, The $[Fe'] \times [CO_3^{2-}]$ synergistic interaction is also observed in CO_2-manipulated natural seawater. Data are mean ± s.e.m.; $n = 3$ biological replicates; $n = 27$ individual experiments; linear regression $P = 6 \times 10^{-9}$.

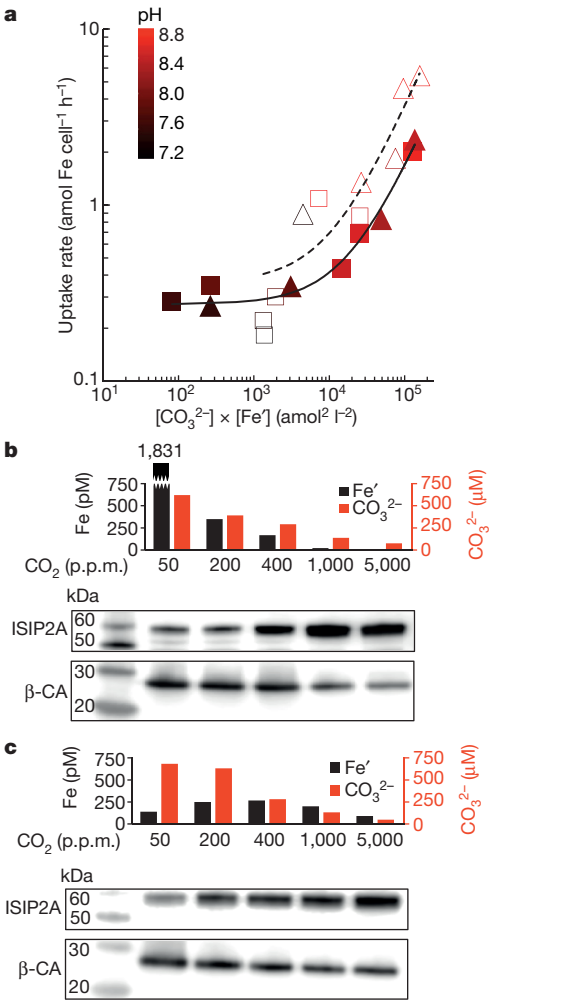

Figure 4 | pH and CO_2 manipulation of *P. tricornutum* induces expression of ISIP2A. a, In *P. tricornutum* cultures, elevated CO_2 lowers pH, decreasing both $[CO_3^{2-}]$ and $[Fe']$ and resulting in decreased ^{59}Fe′ uptake rates (filled shapes and solid line). $n = 9$ individual experiments; linear regression $P = 5 \times 10^{-8}$. Constraining the change in $[Fe']$ relative to $[CO_3^{2-}]$ confirms the influence of $[CO_3^{2-}]$ on uptake rates (open shapes, dashed line). $n = 10$ individual experiments, linear regression $P = 2 \times 10^{-5}$. **b**, Immunoblots of ISIP2A and β-carbonic anhydrase (β-CA) for conditions in which the change in $[CO_3^{2-}]$ and $[Fe']$ is unconstrained (solid triangles from **a**). **c**, Immunoblots of ISIP2A and β-carbonic anhydrase for conditions in which the change in $[Fe']$ is constrained in relation to the change in $[CO_3^{2-}]$ (open triangles from **a**). Graphs indicates $[Fe']$, $[CO_3^{2-}]$ and bubbled CO_2 per immunoblot, β-carbonic anhydrase was used as carbon chemistry indicator. Immunoblot experiments were replicated three times with independent cultures, each with equivalent results.

acids can replace CO_3^{2-} in an anion–Fe–transferrin ternary complex[22], evidence for *in vivo* iron assimilation is rare[23], and a panel of surrogate anions failed to restore *P. tricornutum* uptake rates (Fig. 3c). When cells are resuspended in natural seawater, the synergistic interaction between Fe′ and CO_3^{2-} is also observed, further supporting carbonate ion as the most likely Fe-coordinating anion (Fig. 3d). The correlation between Fe′ uptake rates and $[CO_3^{2-}]$ occurs at environmentally relevant concentrations of CO_3^{2-}, indicating that $[CO_3^{2-}]$ co-limits Fe′ uptake, and suggesting that the projected decline in seawater $[CO_3^{2-}]$ due to ocean acidification could negatively affect phytotransferrin-mediated iron acquisition[24].

To investigate the effects of acidification on Fe′ uptake rates, we aerated cultures of *P. tricornutum* with 50–5,000 p.p.m. CO_2, generating cultures in which the pH ranged from 8.7 to 7.2 (Extended Data Table 3). In seawater, acidification increases $[H^+]$ and decreases $[CO_3^{2-}]$, two linked processes that separately influence each component of the synergistic interaction between Fe′ and CO_3^{2-}. In seawater in which $[Fe']$ is buffered with EDTA, the increase in $[H^+]$ decreases the favourability of Fe–EDTA dissociation[25]. Therefore, as pH decreases, $[Fe']$ decreases, and this change in iron chemistry has been documented to decrease *P. tricornutum* uptake rates[26]. However, here we show that the interactive effect between CO_3^{2-} and Fe′ in determining uptake rates is significant ($P = 0.00375$), with the $[Fe'] \times [CO_3^{2-}]$ product resulting in a better uptake model than $[Fe']$ alone (Fig. 4, solid line, and Extended Data Fig. 5b, c). Our results show that the effects of acidification are two-edged: whereas low pH decreases $[Fe']$, low $[CO_3^{2-}]$ decreases Fe′ bioavailability, and both of these processes act individually and in tandem to reduce phytotransferrin-mediated iron uptake rates.

High expression levels of ISIP2A are an indication of iron-limited growth[6], and in the high-CO_2 cultures, ISIP2A expression may be responding to $[Fe']$, $[CO_3^{2-}]$ or both (Fig. 4b). To demonstrate that changes in $[CO_3^{2-}]$ can induce the expression of ISIP2A, we constrained the change in $[Fe']$ by altering the Fe:EDTA ratio (Extended Data Table 4). We show that ^{59}Fe uptake rates are correlated with changes in $[CO_3^{2-}]$, but not with changes in $[Fe']$ (Extended Data Fig. 5d, e). As in the $NaHCO_3$-manipulation experiments, the interaction between Fe′ and CO_3^{2-} remained a significant model for predicting Fe′ uptake rates (Fig. 4a, dashed line), confirming that elevated CO_2 decreases the bioavailability of Fe′ and induces the expression of ISIP2A (Fig. 4c). This link between CO_2 and iron acquisition resolves the puzzling

© 2018 Macmillan Publishers Limited, part of Springer Nature. All rights reserved.

Fe–CO_2 co-regulation of FEA1 (also known as H43), an algal iron-binding protein[27] that was initially identified during high-CO_2 cultivation of the chlorophyte *Chlorococcum littorale*[28]. Our placement of FEA1 in the phytotransferrin family provides a biochemical basis for the observed influence of CO_2 on iron homeostasis while validating the CO_2 sensitivity of phytotransferrin in distantly related taxa (Fig. 1).

The requirement for synergistic binding reveals the existence of a previously undescribed form of iron–carbonate co-limitation[29] that may be relevant in environments in which primary productivity is limited by [Fe]. Like transferrin, phytotransferrin exploits carbonate chemistry to function as both coordination anion and internalization release trigger[13], resulting in a mechanism that is exquisitely sensitive to acidification-induced changes in [CO_3^{2-}]. Our results show that under constant [Fe′], the doubling of CO_2 to 800 p.p.m. CO_2 can reduce *P. tricornutum* Fe′ uptake rates by 44%. While Fe′ is an important component of phytoplankton nutrition[5], we also show that *P. tricornutum* can use phytotransferrin-independent pathways to access organically complexed iron. In the marine environment, this pool of complexed iron is much larger[3], although uptake rates can be orders of magnitude slower[30], underscoring the trade-off inherent to the different iron acquisition strategies. As iron-limited regions exert an important influence on global biogeochemical cycles[1], we view these results as a starting point for understanding the complex and interdependent influences of ocean acidification on phytoplankton iron uptake mechanisms and rates.

Online Content Methods, along with any additional Extended Data display items and Source Data, are available in the online version of the paper; references unique to these sections appear only in the online paper.

Received 30 January 2017; accepted 5 February 2018.
Published online 14 March 2018.

1. Moore, C. M. *et al.* Processes and patterns of oceanic nutrient limitation. *Nat. Geosci.* **6,** 701–710 (2013).
2. Boyd, P. W. *et al.* Mesoscale iron enrichment experiments 1993–2005: synthesis and future directions. *Science* **315,** 612–617 (2007).
3. Gledhill, M. & Buck, K. N. The organic complexation of iron in the marine environment: a review. *Front. Microbiol.* **3,** 69 (2012).
4. Barbeau, K., Rue, E. L., Bruland, K. W. & Butler, A. Photochemical cycling of iron in the surface ocean mediated by microbial iron(III)-binding ligands. *Nature* **413,** 409–413 (2001).
5. Morel, F. M. M., Kustka, A. B. & Shaked, Y. The role of unchelated Fe in the iron nutrition of phytoplankton. *Limnol. Oceanogr.* **53,** 400–404 (2008).
6. Allen, A. E. *et al.* Whole-cell response of the pennate diatom *Phaeodactylum tricornutum* to iron starvation. *Proc. Natl Acad. Sci. USA* **105,** 10438–10443 (2008).
7. Lommer, M. *et al.* Genome and low-iron response of an oceanic diatom adapted to chronic iron limitation. *Genome Biol.* **13,** R66 (2012).
8. Morrissey, J. *et al.* A novel protein, ubiquitous in marine phytoplankton, concentrates iron at the cell surface and facilitates uptake. *Curr. Biol.* **25,** 364–371 (2015).
9. Marchetti, A. *et al.* Comparative metatranscriptomics identifies molecular bases for the physiological responses of phytoplankton to varying iron availability. *Proc. Natl Acad. Sci. USA* **109,** E317–E325 (2012).
10. Bertrand, E. M. *et al.* Phytoplankton–bacterial interactions mediate micronutrient colimitation at the coastal Antarctic sea ice edge. *Proc. Natl Acad. Sci. USA* **112,** 9938–9943 (2015).
11. Lambert, L. A., Perri, H., Halbrooks, P. J. & Mason, A. B. Evolution of the transferrin family: conservation of residues associated with iron and anion binding. *Comp. Biochem. Physiol.* **142,** 129–141 (2005).
12. Aisen, P., Leibman, A. & Zweier, J. Stoichiometric and site characteristics of the binding of iron to human transferrin. *J. Biol. Chem.* **253,** 1930–1937 (1978).
13. Baker, H. M., Anderson, B. F. & Baker, E. N. Dealing with iron: common structural principles in proteins that transport iron and heme. *Proc. Natl Acad. Sci. USA* **100,** 3579–3583 (2003).
14. Fisher, M., Gokhman, I., Pick, U. & Zamir, A. A structurally novel transferrin-like protein accumulates in the plasma membrane of the unicellular green alga *Dunaliella salina* grown in high salinities. *J. Biol. Chem.* **272,** 1565–1570 (1997).
15. Anderson, M. A. & Morel, F. M. The influence of aqueous iron chemistry on the uptake of iron by the coastal diatom *Thalassiosira weissflogii*. *Limnol. Oceanogr.* **27,** 789–813 (1982).
16. Bruns, C. M. *et al.* Structure of *Haemophilus influenzae* Fe^{+3}-binding protein reveals convergent evolution within a superfamily. *Nat. Struct. Biol.* **4,** 919–924 (1997).
17. Och, L. M. & Shields-Zhou, G. A. The Neoproterozoic oxygenation event: environmental perturbations and biogeochemical cycling. *Earth Sci. Rev.* **110,** 26–57 (2012).
18. Smith, S. R. *et al.* Transcriptional orchestration of the global cellular response of a model pennate diatom to diel light cycling under iron limitation. *PLoS Genet.* **12,** e1006490 (2016).
19. Karas, B. J. *et al.* Designer diatom episomes delivered by bacterial conjugation. *Nat. Commun.* **6,** 6925 (2015).
20. Harding, C., Heuser, J. & Stahl, P. Receptor-mediated endocytosis of transferrin and recycling of the transferrin receptor in rat reticulocytes. *J. Cell Biol.* **97,** 329–339 (1983).
21. Fisher, M., Zamir, A. & Pick, U. Iron uptake by the halotolerant alga *Dunaliella* is mediated by a plasma membrane transferrin. *J. Biol. Chem.* **273,** 17553–17558 (1998).
22. Schlabach, M. R. & Bates, G. W. The synergistic binding of anions and Fe^{3+} by transferrin. Implications for the interlocking sites hypothesis. *J. Biol. Chem.* **250,** 2182–2188 (1975).
23. Halbrooks, P. J., Mason, A. B., Adams, T. E., Briggs, S. K. & Everse, S. J. The oxalate effect on release of iron from human serum transferrin explained. *J. Mol. Biol.* **339,** 217–226 (2004).
24. Doney, S. C., Fabry, V. J., Feely, R. A. & Kleypas, J. A. Ocean acidification: the other CO_2 problem. *Annu. Rev. Mar. Sci.* **1,** 169–192 (2009).
25. Sunda, W. & Huntsman, S. Effect of pH, light, and temperature on Fe–EDTA chelation and Fe hydrolysis in seawater. *Mar. Chem.* **84,** 35–47 (2003).
26. Shi, D., Xu, Y., Hopkinson, B. M. & Morel, F. M. M. Effect of ocean acidification on iron availability to marine phytoplankton. *Science* **327,** 676–679 (2010).
27. Allen, M. D., del Campo, J. A., Kropat, J. & Merchant, S. S. FEA1, FEA2, and FRE1, encoding two homologous secreted proteins and a candidate ferrireductase, are expressed coordinately with FOX1 and FTR1 in iron-deficient *Chlamydomonas reinhardtii*. *Eukaryot. Cell* **6,** 1841–1852 (2007).
28. Sasaki, T., Kurano, N. & Miyachi, S. Cloning and characterization of high-CO_2-specific cDNAs from a marine microalga, *Chlorococcum littorale*, and effect of CO_2 concentration and iron deficiency on the gene expression. *Plant Cell Physiol.* **39,** 131–138 (1998).
29. Saito, M. A., Goepfert, T. J. & Ritt, J. T. Some thoughts on the concept of colimitation: three definitions and the importance of bioavailability. *Limnol. Oceanogr.* **53,** 276–290 (2008).
30. Lis, H., Shaked, Y., Kranzler, C., Keren, N. & Morel, F. M. M. Iron bioavailability to phytoplankton: an empirical approach. *ISME J.* **9,** 1003–1013 (2015).

Supplementary Information is available in the online version of the paper.

Acknowledgements We thank J. Badger for early contributions to phylogenetic analyses, A. Dickson for pH analysis, K. Forsch for CSV measurements and E. Bertrand for trace-metal clean techniques. This study was supported by the National Science Foundation (NSF-MCB-1024913, NSF-ANT-1043671 and NSF-OCE-0727997), United States Department of Energy Genomics Science program (DE-SC00006719 and DE-SC0008593), and the Gordon and Betty Moore Foundation grant GBMF3828 (A.E.A.); NSF-1557928 (A.B.K.); and the Czech Science Foundation, project 15-17643S (M.O. and A.H.).

Author Contributions J.B.M., A.B.K., M.O. and A.E.A. designed the study and interpreted the results. J.B.M., M.O. and A.H. generated and analysed phylogenetic and molecular clock data. J.B.M. and B.J.K. generated mutant cell lines, J.B.M. and A.B.K. with assistance from K.A.B. performed physiology experiments. J.B.M. performed microscopy, and H.Z. performed western blots. T.K. and A.J.A. analysed inorganic carbon species. J.B.M. and J.P.M. conducted statistical analyses. J.B.M. wrote the paper with input from A.E.A., A.B.K., M.O., J.P.M, A.J.A. and K.A.B. All authors discussed the results and commented on the manuscript.

Author Information Reprints and permissions information is available at www.nature.com/reprints. The authors declare no competing interests. Readers are welcome to comment on the online version of the paper. Publisher's note: Springer Nature remains neutral with regard to jurisdictional claims in published maps and institutional affiliations. Correspondence and requests for materials should be addressed to A.E.A. (aallen@jcvi.org).

Reviewer Information *Nature* thanks S. Amin, E. DeLong and the other anonymous reviewer(s) for their contribution to the peer review of this work.

© 2018 Macmillan Publishers Limited, part of Springer Nature. All rights reserved.

METHODS

Phylogenetic analysis. To maximize the dimensions of our phylogenetic analysis, we built a series of hidden Markov models (HMM) from manually curated multiple peptide alignments. HMMs were assembled using transferrin and ISIP2A sequences obtained from NCBI via BLAST. Transferrin and ISIP2A HMMs were then used to iteratively obtain sequences from the Marine Microbial Eukaryote Transcriptome Sequencing Project (MMETSP)[31]. For inclusion into the transferrin and phytotransferrin clades, sequences were manually screened to ensure that they contained the conserved metal-binding residues and the carbonate-binding region (Extended Data Fig. 1a). Sequences were aligned using the genafpair exhaustive algorithm included in MAFFT[32]. The alignment was then manually inspected and ambiguous regions were removed in SEAVIEW v.4[33]. Phylogenetic analysis was conducted using maximum likelihood under the gamma-corrected LG matrix in RAxML v.8.2.8[34]. The best topology, as well as non-parametric branching support was inferred using fast algorithm (-f a option) from 1,000 replicates. Owing to the high divergence of the sequences, we have alternatively used Bayesian inference under the probabilistic CAT algorithm with numbers of site categories limited to 40 (C40 model), combined with empirical exchange rates as defined by the LG model in PhyloBayes v.4.1[35]. Two independent Markov chain Monte Carlo (MCMC) chains were run until they converged (that is, maximum observed discrepancy was below 0.2) and minimum effective size of model parameters exceeded 100.

Divergence time estimation. Fossil calibration points for multicellular taxa (metazoans and green plants) were compiled from http://fossilcalibrations.org (Extended Data Table 4). Calibration of diatoms and haptophytes (mineralizing protozoans) was adopted according previously published studies[36,37]. Respective values are summarized in Supplementary Table 4. The best-scoring topology from the Bayesian inference (see above) was then used for an estimation of divergence using UGAM and CIR relaxed clock models in PhyloBayes v.4.1. In addition, we used an uncorrelated log-normal clock model as implemented in BEAST v.2[38]. For this model, MCMC was run for 30 million generations. Convergence as well as effective sample size was evaluated using Tracer and the dating visualized on the tree using TreeAnnotator in the BEAST package.

Predictions of signal peptides, transmembrane domains and glycosylphosphatidylinositol anchors. All the sequences used for phylogenetic reconstructions were searched for the presence of signal peptide, transmembrane domains and glycosylphosphatidylinositol anchor (GPI). Endoplasmic reticulum signal peptides were predicted using SignalP[39] and TargetP[40,41]. Transmembrane domains were searched using TMHMM[42] and GPI anchors were predicted by PredGPI[43]. The results are shown in Supplementary Table 2.

Cell lines and cultivation. All cultivation and manipulation of *P. tricornutum* strain CCMP 632 was conducted using sterile trace-metal clean techniques and in Aquil medium[44], unless otherwise noted. To remove contaminating iron, prepared medium was first passed through a Chelex 100 resin (Bio-Rad Laboratories) and microwave-sterilized in acid-cleaned polycarbonate bottles before addition of filter-sterilized, Chelex-passaged nutrient stocks and F/2 vitamin supplements.

Cultures for short-term ^{59}Fe uptake rate experiments. Cultures were grown in medium supplemented with macronutrients (880 μM NO_3, 36 μM PO_4, 106 μM SiO_4) and trace metals (100 nM Zn, 48 nM Mn, 40 nM Co, 40 nM Cu, 10 nM Se and 100 nM Ni) with 100 μM EDTA. Vitamin and metal–EDTA solutions were added to artificial seawater and allowed to equilibrate overnight. Iron was pre-equilibrated overnight in a 1:1.25 ratio of iron:EDTA before addition. Cultures were maintained at 17 °C at 300 μmol quanta m^{-2} s^{-1} in a 10-h:14-h dark:light cycle, and all culture manipulations were done under a class-100 HEPA filter. Background contaminating iron was measured by flow injection analysis at multiple times and varied from 0.2–0.7-nM dissolved iron over the two-year course of experiments. Fe′, the sum of all labile inorganic iron species, was calculated as previously described[44].

Cultures grown for growth rate analysis. Cultures of *P. tricornutum* (CCMP 632) were grown in a modified Aquil medium[44] containing EDTA, Co, Cu, Mo, Mn and Zn at final concentrations of 3×10^{-4} M, 1.51×10^{-7} M, 1×10^{-7} M, 3.36×10^{-7} M, 1×10^{-8} M and 2.39×10^{-7} M, with variable Fe concentrations. Cells were grown at 320 μmol photons m^{-2} s^{-1} under a 12-h:12-h light:dark cycle using cool-white fluorescent bulbs. Under these conditions, Fe′ = 0.00068 of total Fe. A maximum of 700 pmol l^{-1} Fe′ was assumed, because of iron hydroxide precipitation, but for simplicity, we report the results as Fe′ even at concentrations exceeding this maximum. Cell growth was monitored daily using a Turner AU-10 fluorometer for *in vivo* chlorophyll fluorescence, and steady-state growth rates were computed from linear regressions of ln(relative fluorescence) versus time.

TALEN knockouts, transferrin complementation and site-directed mutagenesis. Transcription activator-like effector nucleases (TALENs) were used to disrupt the *ISIP2A* gene. TALEN construction protocols followed the methods as described for *P. tricornutum*[49]. In brief, a unique pair of 20-nucleotide length sequences was designed to span the first intron junction of ISIP2A (GenBank ID: XP_002179762.1). TALEN constructs were assembled into the pTH vector[49] and the sequence was verified. A homologous recombination (HR) plasmid containing resistance to nourseothricin and driven by the promoter/terminator for the light harvesting promoter *FcpA*[45] was assembled into pUC-19 using Gibson cloning[46]. Both HR and pTH plasmids were introduced into *P. tricornutum* via particle bombardment[47]. Transformants were pre-screened by PCR for correct insertion of the nourseothricin-resistance cassette and *ΔISIP2A* gene knockouts were subsequently confirmed by western blot using custom-made Genomic Antibodies (OriGene) targeting the ISIP2A protein. Complementary sequences for the N- and C-terminal domains of hTF were codon-optimized for the diatom *Thalassiosira pseudonana* and designed using CLC software (Qiagen), and the signal peptide and C-terminal transmembrane anchor of ISIP2A were subsequently added before synthesis. The fusion products were then synthesized on a BioXp 3200 DNA synthesizer (SGI DNA). YFP was fused via Gibson cloning to the signal and transmembrane sequences of ISIP2A, while the ISIP2A complement was obtained by amplifying *P. tricornutum* cDNA (GeneScript). PCR-based site-directed mutagenesis strains were made with base-pair mismatch primers and amplified from the ISIP2A complement strain. All constructs were placed under control of the *P. tricornutum* nitrate reductase promoter and terminator[19,48], sequence-verified, and maintained on pUC-19 vectors ($n = 3$ for each construct). All complement sequences were Gibson-assembled into the cargo plasmid p0521s[19] (containing a selection marker for bleomycin) and introduced into the *ΔISIP2A*-knockout strain via conjugation with *Escherichia coli* Epi300 cells as previously described[49]. Positive transformants were selected on dual nourseothricin/zeocin antibiotic plates (200 and 100 μg ml^{-1}, respectively) and verified by PCR and sequencing. Cell lines were maintained in 7.5 nM Fe–EDTA Aquil medium under positive antibiotic selection until testing.

Short-term ^{59}Fe uptake assays. Cell strains were grown without antibiotic selection and acclimatized in Aquil medium at 15 pM Fe′ for a minimum of five transfers before assay. Growth in 15 pM Fe′ was found to reduce the growth rate in wild-type *P. tricornutum* by approximately 15%, with an approximate F_v/F_m of 0.55, indicative of iron-limited (but not iron-starved) growth[6]. Cell counts were conducted on a Beckman Quanta cell cytometer and cross-calibrated by direct microscopic counts using a haemocytometer. To avoid changes to physiology and medium pH, cultures were grown and assayed at low cell densities ($1–3 \times 10^5$ cells ml^{-1}). ^{59}Fe was equilibrated with EDTA at a 1:2 ratio and pH 7 for 24 h before use. The specific activity of the ^{59}Fe was 42 Ci g^{-1}, or about 0.08% pure. Desferrioxamine B (DFB) was complexed with ^{59}Fe by equilibrating at pH 3 overnight and adjusting to pH 8 with high-purity NaOH. The ratio of ^{59}Fe to uncomplexed DFB was 4:5. Precomplexed ^{59}Fe–EDTA and ^{59}Fe–DFB substrates were added to standard medium containing 100 μM EDTA and allowed to equilibrate overnight. Uptake assays were commenced by gravimetrically adding a 1:10 volume to the cell cultures. Uptake assay data were generated from uptake curves consisting of a minimum of five time points spaced 20–30 min apart. Assays were simultaneous and staggered, resulting in variations in the total length of assay; however, assays were no less than 2 h in length, and did not exceed 3 h in duration. ISIP2A protein expression has a strong diurnal pattern: for consistency and reproducibility, cells were collected in the light portion of the light:dark cycle. Room temperature fluctuations influence both carbon and iron speciation; temperature changes were accounted for in calculating Fe:EDTA dissociation constants[25] and CO_2 speciation[54]. During uptake assays, cells were shielded from actinic light and periodically filtered onto 2.0-μm PTFE filters, washed with Ti–citrate–EDTA solution[50] and preserved in Ecolite (MP Biomedicals) before liquid scintillation counting.

Carbonic acid system manipulation and surrogate anion experiments. Medium for the carbonic acid manipulation experiments was made by acidifying Chelex-treated bicarbonate-free Aquil medium to pH 3 with ultra-high purity HCl and bubbling with filtered N_2 for 60 min to strip out dissolved CO_2. To buffer against large (±0.1 pH) changes in pH, Chelex-treated Tris-HCl was added at a final concentration of 2 mM, and the pH was adjusted back to 8.0 using ultra-high purity ammonium hydroxide. Ammonium hydroxide was used rather than sodium hydroxide to avoid contaminating the uptake medium with sodium bicarbonate, which is a common atmospherically derived contaminant in NaOH. Trace-metal clean F/2 nutrients were added, and all medium was stored in an N_2/O_2-purged, CO_2-impermeable glove box before use. Carbonate ion availability was manipulated by adding $NaHCO_3$ to sub-aliquoted bottles of medium at concentrations of 0, 0.5, 1, 1.5, 2, 4 and 6 mM $NaHCO_3$ l^{-1}, and allowed to equilibrate 24 h. ^{59}Fe–EDTA or ^{59}Fe–FOB were added 24 h before assay and allowed to equilibrate. *P. tricornutum* cells were grown in 2.7-l square polycarbonate bottles in Aquil medium containing 15 pM Fe′ (7.5 nM Fe–EDTA), and were grown on a 10-h:14-h light:dark schedule. Cultures were grown to early exponential phase (3×10^5 cells ml^{-1}) and collected

© 2018 Macmillan Publishers Limited, part of Springer Nature. All rights reserved.

by centrifugation for 30 min at 1,000*g* at 17 °C in acid-cleaned centrifuge bottles. Cells were washed and centrifuged twice in $NaHCO_3$-free Aquil synthetic seawater salts (without nutrients), and re-suspended in the carbonate chemistry-adjusted ^{59}Fe medium. Uptake reaction volume was 150 ml, and to avoid unnecessary aeration, the medium was removed from the medium bottles using an acid-cleaned pipette. Volumes were determined gravimetrically. Uptake rates were assayed as outlined above (5-point curves, 2–3 h in duration), and samples for pH and total dissolved inorganic carbon (DIC) analysis removed from parallel (non-radioactive) cultures, poisoned with $HgCl_2$, sealed with Apiezon-L vacuum grease (M&I Materials) and stored in borosilicate-stoppered bottles for analysis[51]. Owing to the presence of Tris-HCl, total alkalinity was not analysed for this experiment and inorganic carbon speciation was calculated from pH and DIC (see below).

To test whether other anions could substitute for carbonate ions, bicarbonate-free medium was prepared as above. Sub-aliquots of this medium were used to create 100 mM stocks of the sodium salts of formate, acetate, oxalate, glycolate and pyruvate. These stocks were Chelex-treated for 48 h at 4 °C before use. These alternate anion stocks were diluted 1:1,000 into 150-ml uptake medium reactions and the medium was allowed to equilibrate in an N_2/O_2-purged, CO_2-impermeable glove box as above. Cells were grown, collected and resuspended as above, and added to the 150-ml uptake reactions. Uptake rates were assayed as in the previous carbonic acid manipulation experiments: 5-point assay curves with a total uptake assay length of 2–3 h. Samples for pH and DIC analysis were removed from parallel (non-radioactive) cultures, poisoned with $HgCl_2$, sealed with Apiezon-L vacuum grease (M&I Materials) and stored in borosilicate-stoppered bottles for analysis[51]. Carbonate contamination in the unsupplemented control was 2.5 μM (Extended Data Table 2).

Demonstration of carbonate effect in natural seawater. On 16 January 2013, seawater was collected from 3 m depth at the edge of the sea ice in McMurdo Sound Ross Sea, Antarctica (77° 36.999′ S 165° 28.464′ E). Water was pumped to the surface using a trace-metal clean diaphragm pump via acid-cleaned Teflon tubing and filtered on-site through an acid-cleaned 0.22-μm filter. Filtered seawater was dispensed into trace-metal clean 50-l carboys and stored in the dark at 4 °C. Phytoplankton grown in this batch of seawater are iron-limited[10]. For North Pacific Gyre water, seawater from station ALOHA (22° 45′ N 158° 00′ W) was collected in June 2016 using trace-metal clean techniques and similarly filtered and cold-stored before use. Samples of both types of natural seawater plus synthetic seawater (Aquil) were dispensed into 2.7-l acid-cleaned polycarbonate bottles. Seawater was amended with 100 μM EDTA and Chelex-treated F/2 nutrients and allowed to equilibrate overnight. Two-litre samples of seawater were placed in 2.7-l acid-cleaned polycarbonate bottles and bubbled with filtered N_2/O_2 mixtures containing 200 and 1,000 p.p.m. CO_2. Tubing and lines were acid-cleaned PTFE, with acid-soaked and -cleaned plastic aerators (Lee's Discard-a-Stone) used to maximize gas transfer. One hundred and fifty millilitres of each seawater sample (CO_2-modified samples and the unmodified controls) was transferred to small polycarbonate bottles as uptake medium, with 7.5 nM ^{59}Fe–EDTA allowed to equilibrate overnight. Separately, *P. tricornutum* was grown in 7.5 nM Fe–EDTA Aquil to early exponential phase (3×10^5 cells ml^{-1}) and harvested by centrifugation for 30 min at 1,000*g* at 17 °C in acid-cleaned centrifuge bottles. This concentrate was resuspended in the uptake medium, and uptake rates were assayed as outlined above (5 point curves, 2–3 h in duration), and samples for total alkalinity and DIC analysis removed from parallel (non-radioactive) cultures, poisoned with $HgCl_2$, sealed with Apiezon-L vacuum grease (M&I Materials), and stored in borosilicate-stoppered bottles for analysis[51]. This experiment was repeated with three cultures on three separate days.

Approximation of Fe′ and carbonate rate constants ($NaHCO_3$ addition experiments). The short-term uptake rates determined from an iron-limited culture incubated across a range of [CO_3^{2-}] and Fe′ levels (Extended Data Table 1) were used to determine a second-order rate constant for Fe′ uptake and to solve for pseudo-first-order rate constants with respect to Fe′ and [CO_3^{2-}]. These results are expressed on a per-cell basis, and pertain to cultures of *P. tricornutum* grown under this condition[51], as the starting ISIP2A protein content per cell was identical (but unknown) in all short-term uptake experiments. Uptake rates determined from the two treatments to which no $NaHCO_3$ was added were excluded. The slope of uptake versus the product of Fe′ and CO_3^{2-} (1.22×10^{-3} mol Fe cell^{-1} h^{-1} (M Fe′)$^{-1}$ (M CO_3^{2-})$^{-1}$; Extended Data Fig. 6a), was used as the starting condition from which an initial CO_3^{2-} rate constant was determined. Assuming Fe uptake rate is first order with respect to Fe′ at low ^{59}Fe (and supported by the ratios of rates observed at varied Fe′ at identical [CO_3^{2-}]), the uptake rates measured at Fe′ ranging from 2 to 45 pM (Extended Data Fig. 6b) and at variable [CO_3^{2-}] were collapsed by dividing these rates by the Fe′ levels (Extended Data Fig. 6d). The slope of this quantity versus [CO_3^{2-}] revealed an initial constant for Fe′-normalized Fe uptake of 1.27×10^{-3} mol Fe cell^{-1} h^{-1} (M CO_3^{2-})$^{-1}$. Then, a pseudo-first-order rate constant of Fe′ for Fe uptake, $k = 0.962$ mol Fe cell^{-1} h^{-1} (M Fe′)$^{-1}$, was estimated from the second-order rate constant and the estimated CO_3^{2-} rate constant. The constituent rate constants for Fe uptake were solved by iteration using these initial conditions. Each round was performed with 16,000 pairs of trial rate constants, allowed to vary randomly from 0.33 to threefold, from the initial or previously iterated values. Residual sum of square values were calculated for each pair of trial rate constants. The median constants from the 20 pairs of trial constants with the lowest residual sum of square values (which had coefficients of variation of 0.01% or less) were used for the next trial. Trials were stopped when constants did not appreciably differ and no trend with trial number was apparent. For each constant, the mean of the last four trials are reported; the iterated constants were 0.782 mol (±0.05) mol Fe cell^{-1} h^{-1} (M Fe′)$^{-1}$ and 0.00156 (±0.00087) mol Fe cell^{-1} h^{-1} (M CO_3^{2-}) for Fe′ and CO_3^{2-}, respectively (about 20% different from initial estimates). The fit of the data using the derived rate constants versus empirically measured rates is shown in Extended Data Fig. 6e.

Carbonic acid system manipulation by CO_2 bubbling, synthetic seawater. Two litres of Chelex-treated Aquil medium in 2.7-l polycarbonate bottles was bubbled with filtered N_2/O_2 mixtures containing 50, 200, 1,000 and 5000 p.p.m. CO_2 plus an ambient air (~400 p.p.m.) control. Tubing and lines were acid-cleaned PTFE, with acid-soaked and -cleaned plastic aerators (Lee's Discard-a-Stone) used to maximize gas transfer. In the first experiment (Fe′ unconstrained), both high (100 nM Fe–EDTA) and low (10 nM Fe–EDTA) Fe′ media were pre-equilibrated with bubbled gas for 48 h before inoculation with a low-iron acclimatized culture of wild-type *P. tricornutum* cells. Cells were monitored twice daily for cell counts, chlorophyll and F_v/F_m. Cultures were grown to a low cell density ($<3 \times 10^5$ cells ml^{-1}) before the uptake assay. The specific growth rates for each culture were determined from the last three cell counts. ^{59}Fe–EDTA was pre-equilibrated overnight in filter-sterilized medium from each culture to assure that medium chemistry would be similar. Assays were a mix of 135 ml culture and 15 ml ^{59}Fe uptake media, blended without aeration, periodically filtered onto 2.0-μm PTFE filters, washed with Ti–citrate–EDTA solution[50] and preserved in Ecolite (MP Biomedicals) before liquid scintillation counting. Short-term uptake assays consisted of a 5-point curve, sampled 20 min apart, and not exceeding 3 h in duration. Culture aliquots of 500 ml were preserved for DIC and total alkalinity, and the rest of the culture was centrifuged and stored for protein expression analysis. Both ISIP2A and β-carbonic anhydrase were analysed on protein-per-cell normalized samples (Invitrogen).

For the Fe′-constrained experiments, the Fe:EDTA ratio was varied to constrain pH-induced changes in [Fe′]. For the low-iron cultures, we attempted to constrain Fe to ~20 pM Fe′ across all five pH and CO_2 manipulations, and in the high-iron cultures, Fe′ was constrained to ~200 pM Fe′. To keep the maximum concentration of EDTA to 1 mM or less, the total concentration of Fe–EDTA was decreased to 50 nM in the Fe-replete cultures, and 10 nM in the Fe-limited cultures. Cultures were analysed as above.

Characterization of endocytosis. To generate fluorescently labelled cell lines, full-length *ISIP2A* and *ISIP1* genes (including the 600 base-pair native promoter and 300-bp native terminator regions) were amplified with Phusion high-fidelity polymerase (New England Biolabs). RFP and YFP protein tags were fused onto constructs using Gibson cloning and assembled into a pUC-19 vector. Full-length constructs were re-amplified, sequence-verified and assembled into p0521s using yeast assembly[22]. Clones were PCR-screened, with positive clones re-sequenced. For microscopy, cells were grown at a low density (2×10^5 cells ml^{-1}) in 7.5 nM Fe–EDTA Aquil medium, centrifuged briefly and resuspended in Aquil medium containing 300 nM Fe–EDTA. Cells were immediately visualized on a Leica SP5 confocal microscope equipped with a 100× oil immersion objective. A 514-nm laser was used to visualize YFP, RFP and plastid autofluorescence, with emission monitored at 520–550 nm, 610–635 nm and 700–740 nm, respectively. The membrane-impermeable dye FM 1-43 was used to stain the outer membrane; wild-type *P. tricornutum* was grown at 7.5 nM Fe–EDTA, centrifuged briefly and resuspended in Aquil medium containing 300 nM Fe–EDTA and 5 μg ml^{-1} of FM 1-43 (Thermo Fisher). Cells were visualized within 10 min of dye addition (excitation 488 nm, emission 610 nm) by confocal microscopy. To evaluate the effect of endocytosis inhibitors, we added 5 μM of the clathrin-mediated endocytosis inhibitor Pitstop2[53] (*N*-[5-(4-bromobenzylidene)-4-oxo-4,5-dihydro-1,3-thiazol-2-yl]-naphthalene-1-sulfonamide, Abcam) to short-term uptake medium containing 7.5 nM Fe–EDTA, mixed and assayed immediately, as outlined above. The toxic effects of Pitstop2 on *P. tricornutum* over the course of the 2-h uptake experiment were not evaluated.

Analysis of seawater carbonate chemistry. Medium samples for pH, total alkalinity and DIC were collected following previously described protocols[51]. All samples were collected in 500-ml Pyrex borosilicate glass bottles and poisoned with 200 μl of a saturated $HgCl_2$ solution to arrest metabolic activity, and bottles were sealed using Apiezon-L sealant. For the $NaHCO_3$-manipulation experiments, pH and

© 2018 Macmillan Publishers Limited, part of Springer Nature. All rights reserved.

DIC were measured: pH was measured on the total pH scale using meta-cresol purple[54], and DIC analyses were carried out using an automated infrared inorganic carbon analyser (AIRICA, Marianda). For the CO_2 bubbling experiments, DIC and total alkalinity were measured. Total alkalinity was determined using an open-cell potentiometric acid titration system equipped with a Metrohm 876 Dosimat Plus automated titrator and a Metrohm Ecotrode Plus pH electrode, as developed by the Dickson Laboratory at Scripps Institution of Oceanography. Performance and accuracy of the analyses was evaluated through analysis of Certified Reference Material provided by the Dickson laboratory. Accuracy and precision ± 2 μmol kg^{-1} was achieved for both DIC and total alkalinity analyses. The complete medium carbonic acid system including carbonate ion concentration was calculated based on pH and DIC ($NaHCO_3$ addition experiment) or DIC and total alkalinity (CO_2 bubbling experiment) data based on *in situ* temperature and salinity using CO2SYS[55].

Statistical analyses. No statistical methods were used to predetermine sample size. All *n* numbers represent biological replicates, and the experiments were not randomized or blinded. All the data in bar graphs are expressed as mean ± s.e.m., with paired Student's *t*-test (two-tailed). The ANOVA interaction effect between variables was used for evaluating synergism[56]. Statistical analysis was performed in R[57], using linear regression (lm), two-way ANOVA (aov) and correlation tests (cor. test), where appropriate, to compare the relationship of Fe′ uptake to [Fe′], [CO_3^{2-}] and the [Fe′] × [CO_3^{2-}] product. Test statistics and *P* values are summarized in Extended Data Table 3. $P < 0.05$ was considered significant.

Data availability. The authors declare that the data supporting the findings of this study are available within the paper and its Supplementary Information.

31. Caron, D. A. *et al.* Probing the evolution, ecology and physiology of marine protists using transcriptomics. *Nat. Rev. Microbiol.* **15,** 6–20 (2017).
32. Katoh, K. & Standley, D. M. MAFFT multiple sequence alignment software version 7: improvements in performance and usability. *Mol. Biol. Evol.* **30,** 772–780 (2013).
33. Gouy, M., Guindon, S. & Gascuel, O. SeaView version 4: a multiplatform graphical user interface for sequence alignment and phylogenetic tree building. *Mol. Biol. Evol.* **27,** 221–224 (2010).
34. Stamatakis, A. RAxML version 8: a tool for phylogenetic analysis and post-analysis of large phylogenies. *Bioinformatics* **30,** 1312–1313 (2014).
35. Lartillot, N., Lepage, T. & Blanquart, S. PhyloBayes 3: a Bayesian software package for phylogenetic reconstruction and molecular dating. *Bioinformatics* **25,** 2286–2288 (2009).
36. Berney, C. & Pawlowski, J. A molecular time-scale for eukaryote evolution recalibrated with the continuous microfossil record. *Proc. R. Soc. B* **273,** 1867–1872 (2006).
37. Parfrey, L. W., Lahr, D. J., Knoll, A. H. & Katz, L. A. Estimating the timing of early eukaryotic diversification with multigene molecular clocks. *Proc. Natl Acad. Sci. USA* **108,** 13624–13629 (2011).
38. Drummond, A. J., Suchard, M. A., Xie, D. & Rambaut, A. Bayesian phylogenetics with BEAUti and the BEAST 1.7. *Mol. Biol. Evol.* **29,** 1969–1973 (2012).
39. Petersen, T. N., Brunak, S., von Heijne, G. & Nielsen, H. SignalP 4.0: discriminating signal peptides from transmembrane regions. *Nat. Methods* **8,** 785–786 (2011).
40. Emanuelsson, O., Nielsen, H., Brunak, S. & von Heijne, G. Predicting subcellular localization of proteins based on their N-terminal amino acid sequence. *J. Mol. Biol.* **300,** 1005–1016 (2000).
41. Nielsen, H., Engelbrecht, J., Brunak, S. & von Heijne, G. Identification of prokaryotic and eukaryotic signal peptides and prediction of their cleavage sites. *Protein Eng.* **10,** 1–6 (1997).
42. Möller, S., Croning, M. D. R. & Apweiler, R. Evaluation of methods for the prediction of membrane spanning regions. *Bioinformatics* **17,** 646–653 (2001).
43. Pierleoni, A., Martelli, P. L. & Casadio, R. PredGPI: a GPI-anchor predictor. *BMC Bioinformatics* **9,** 392 (2008).
44. Sunda, W. G., Price, N. M. & Morel, F. M. M. in *Algal Culturing Techniques* (ed. Anderson. R. A.) 35–63 (Elsevier, 2005).
45. Zaslavskaia, L. A., Lippmeier, J. C., Kroth, P. G., Grossman, A. R. & Apt, K. E. Transformation of the diatom *Phaeodactylum tricornutum* (Bacillariophyceae) with a variety of selectable marker and reporter genes. *J. Phycol.* **36,** 379–386 (2000).
46. Gibson, D. G. *et al.* Enzymatic assembly of DNA molecules up to several hundred kilobases. *Nat. Methods* **6,** 343–345 (2009).
47. Falciatore, A., Casotti, R., Leblanc, C., Abrescia, C. & Bowler, C. Transformation of nonselectable reporter genes in marine diatoms. *Mar. Biotechnol.* **1,** 239–251 (1999).
48. Poulsen, N. & Kröger, N. A new molecular tool for transgenic diatoms: control of mRNA and protein biosynthesis by an inducible promoter–terminator cassette. *FEBS J.* **272,** 3413–3423 (2005).
49. Weyman, P. D. *et al.* Inactivation of *Phaeodactylum tricornutum* urease gene using transcription activator-like effector nuclease-based targeted mutagenesis. *Plant Biotechnol. J.* **13,** 460–470 (2015).
50. Hudson, R. J. M. & Morel, F. M. M. Distinguishing between extra- and intracellular iron in marine phytoplankton. *Limnol. Oceanogr.* **34,** 1113–1120 (1989).
51. Dickson, A. G., Sabine, C. L., & Christian, J. R. (eds) *Guide to Best Practices for Ocean CO_2 Measurements* (North Pacific Marine Science Organization, 2007).
52. Kustka, A. B., Allen, A. E. & Morel, F. M. Sequence analysis and transcriptional regulation of iron acquisition genes in two marine diatoms. *J. Phycol.* **43,** 715–729 (2007).
53. Dutta, D., Williamson, C. D., Cole, N. B. & Donaldson, J. G. Pitstop 2 is a potent inhibitor of clathrin-independent endocytosis. *PLoS ONE* **7,** e45799 (2012).
54. Carter, B. R., Radich, J. A., Doyle, H. L. & Dickson, A. G. An automated system for spectrophotometric seawater pH measurements. *Limnol. Oceanogr. Methods* **11,** 16–27 (2013).
55. Lewis, E., Wallace, D. & Allison, L. J. *Program developed for CO_2 System Calculations* (Carbon Dioxide Information Analysis Center, 1998).
56. Slinker, B. K. The statistics of synergism. *J. Mol. Cell. Cardiol.* **30,** 723–731 (1998).
57. R Core Team. R: A Language and Environment for Statistical Computing. http://www.R-project.org/ (R Foundation for Statistical Computing, Vienna, Austria, 2014).

© 2018 Macmillan Publishers Limited, part of Springer Nature. All rights reserved.

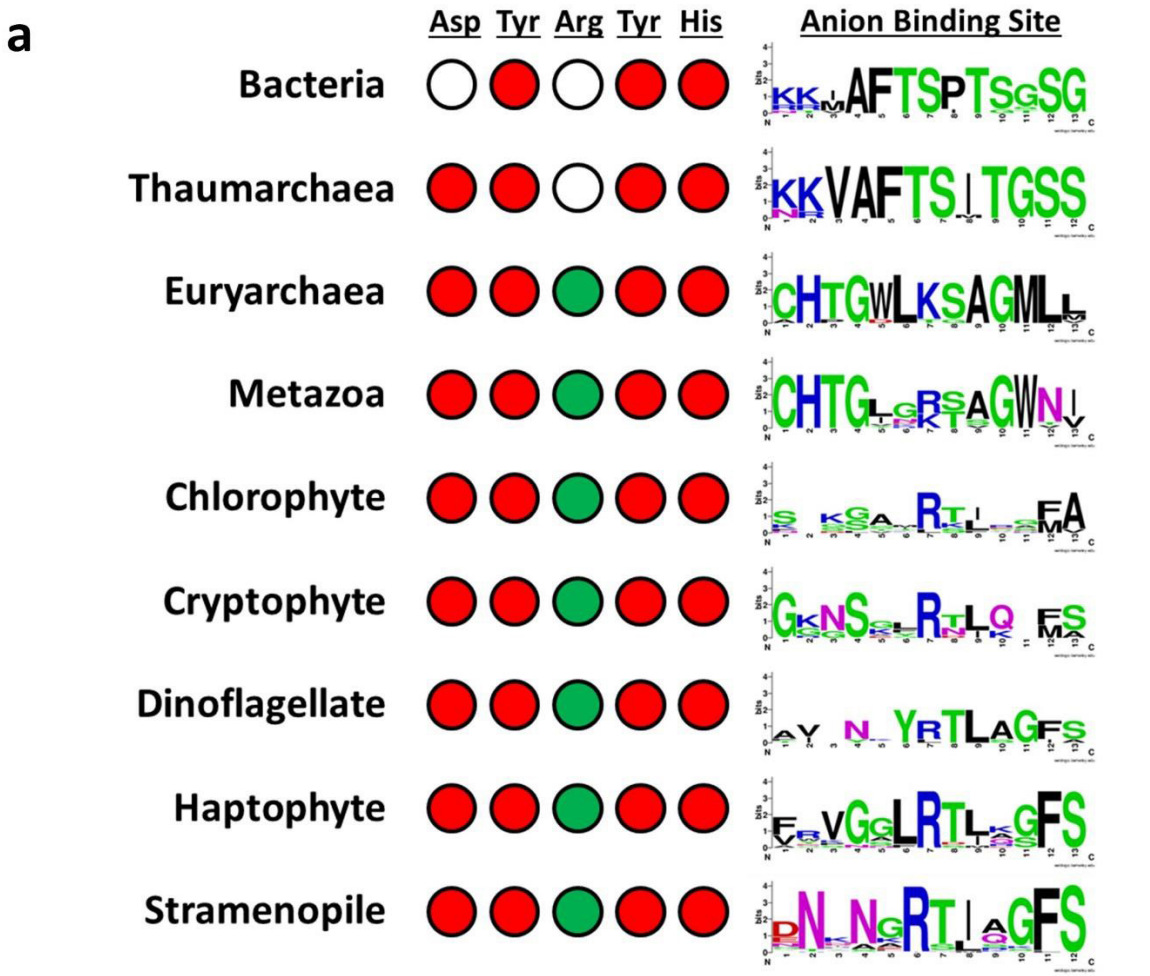

Extended Data Figure 1 | Conservation of active site amino acids. **a**, Left, conservation of putative iron-coordinating (red) and carbonate-coordinating (green) amino acids among phylogenetic groups, filled circles indicate >85% conservation, unfilled circles indicate <20% conservation; arginine and lysine were permitted at the carbonate-binding site[11]. Right, logo tag detailing alignment conservation at the anion-binding region. Phosphonate-binding proteins (Bacteria and Thaumarchaea) retain the S/T-rich phosphonate-binding area, whereas transferrin (Euryarchaea and Metazoa) and phytotransferrin have the carbonate-coordinating K/R insertion. A downstream SAG region used to stabilize carbonate in transferrin[24] shows some conservation in phytotransferrin, but an upstream threonine (−4 amino acids from the conserved Arg) is not present. **b**, Active site homology among ISIP2A (PT54465) and two transmembrane-anchored *P. tricornutum* homologues, PT45708 and PT54466. Amino acid distances based on PT54465, red/green triangles are iron- and carbonate-coordinating amino acids.

© 2018 Macmillan Publishers Limited, part of Springer Nature. All rights reserved.

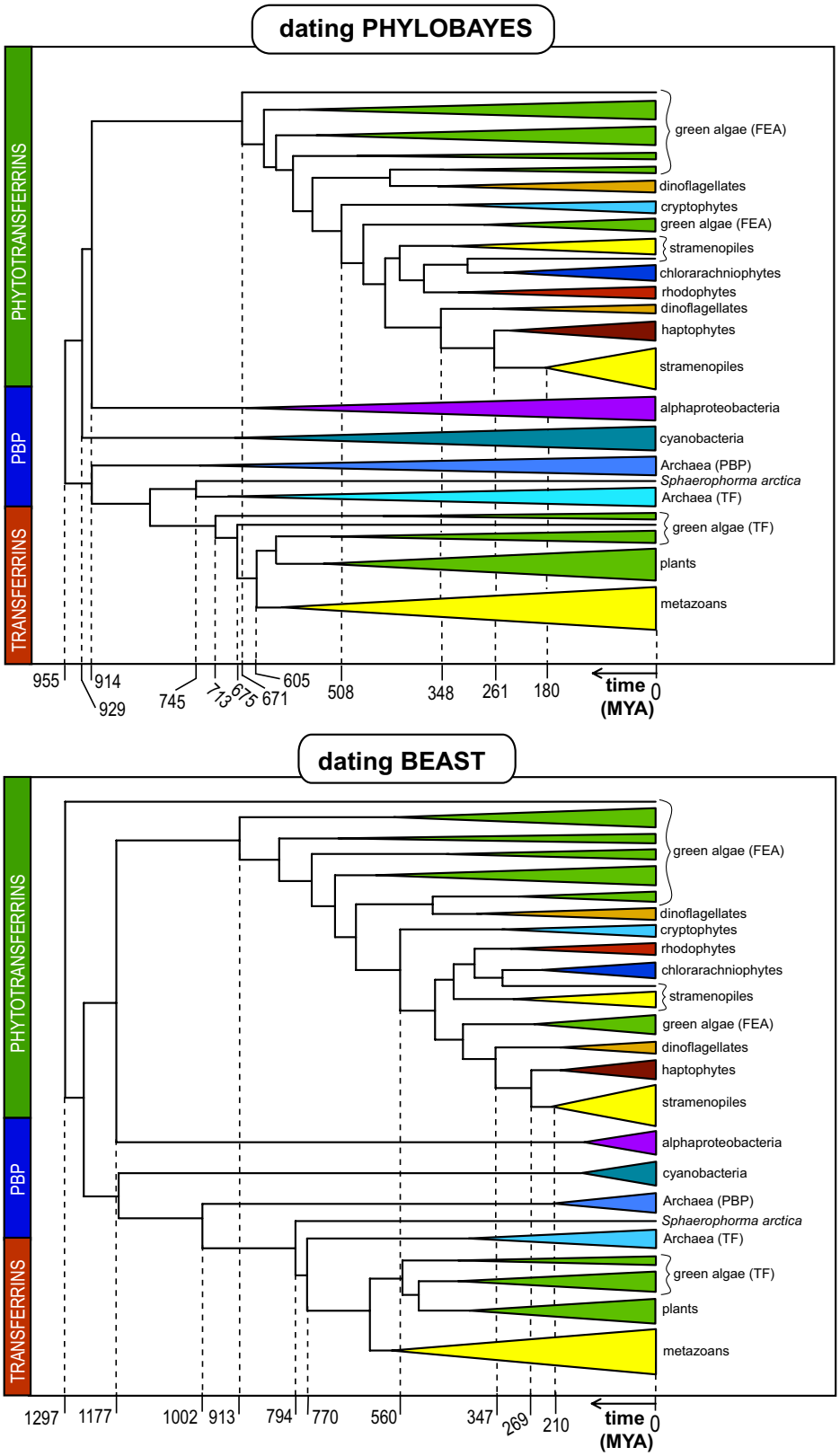

Extended Data Figure 2 | Estimated divergence times between transferrin, phytotransferrin and PBPs. Analyses were carried out using PhyloBayes (top) and BEAST (bottom). For the fossil calibration points used in generating the minimum and maximum constraints, see Supplementary Table 1. MYA, million years ago.

© 2018 Macmillan Publishers Limited, part of Springer Nature. All rights reserved.

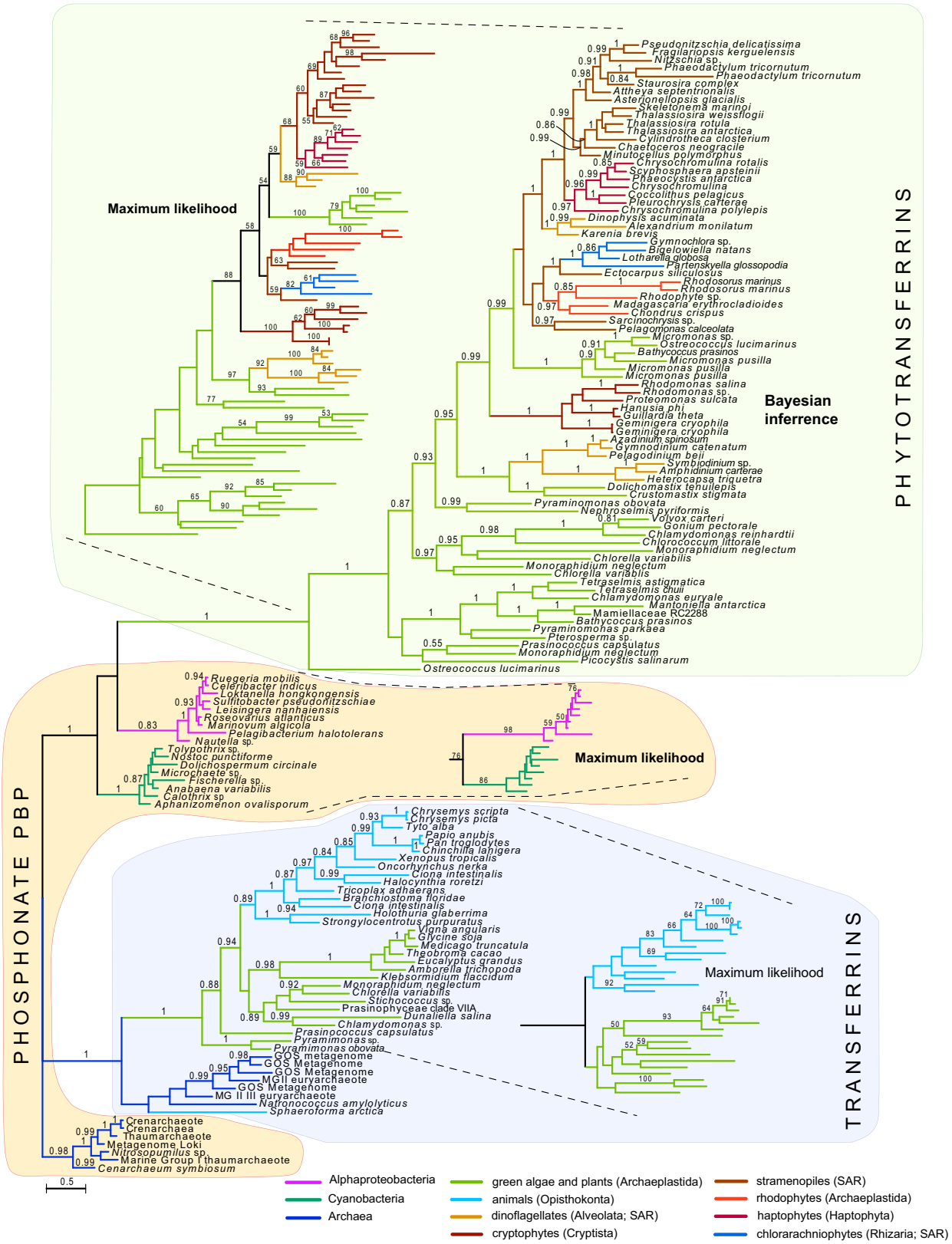

Extended Data Figure 3 | Bayesian (PhyloBayes) phylogenetic tree contrasted with alternate topology derived using maximum likelihood. *Prasinococcus capsulatus*, *Pyraminomonas obovata* and other chlorophyte algae have copies of transferrin and phytotransferrin, whereas all other non-chlorophyte algae have only phytotransferrin. Branches are colour-coded by phylogenetic group. Scale bar, 0.5 substitutions per position.

© 2018 Macmillan Publishers Limited, part of Springer Nature. All rights reserved.

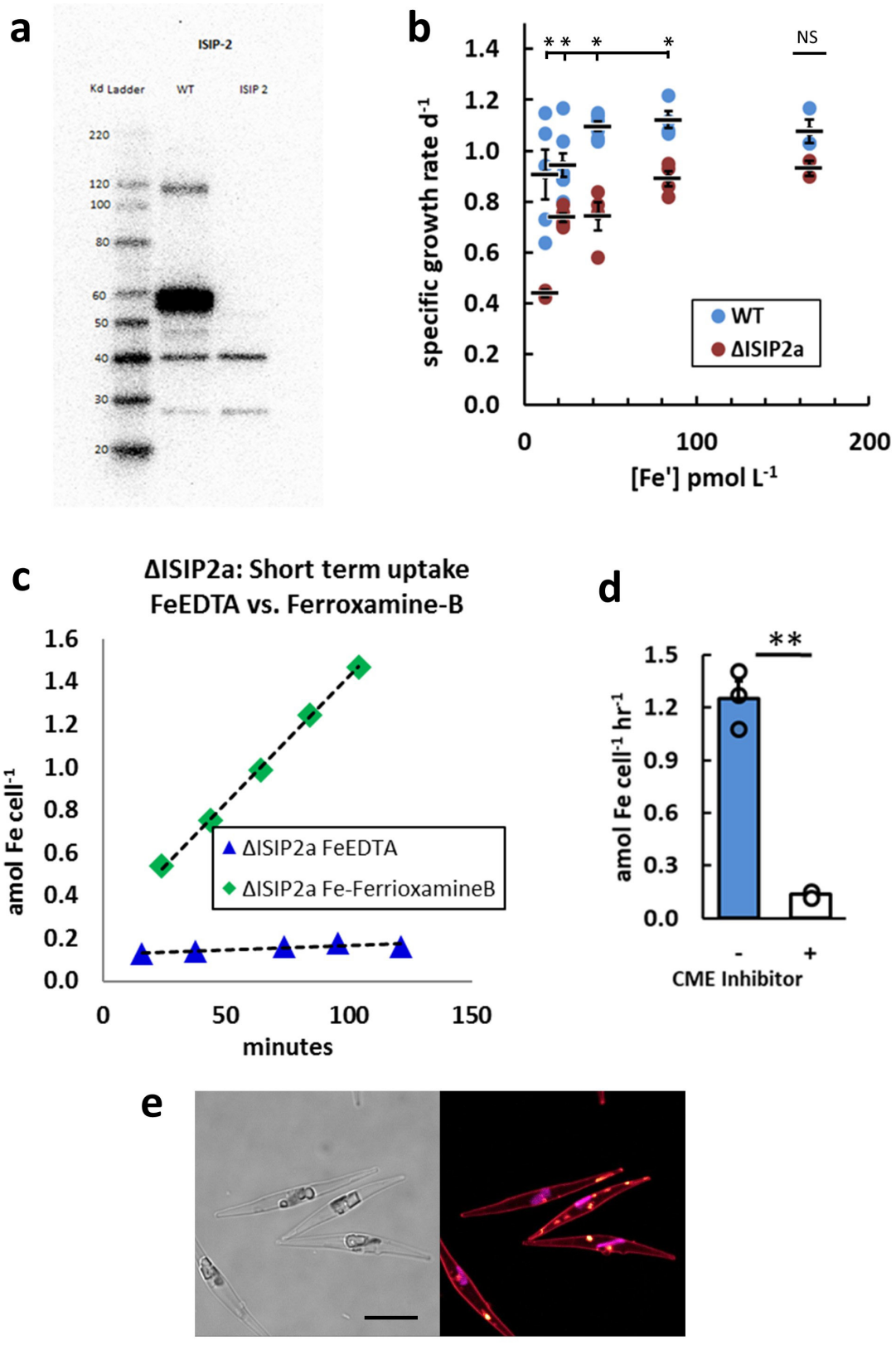

Extended Data Figure 4 | Characterization of ISIP2A. a, Western blot of wild-type *P. tricornutum* compared to *ISIP2A*-knockout strains (*ΔISIP2A*). The estimated mass of ISIP2A protein is 57 kDa. **b**, Specific growth rates of wild type compared to *ΔISIP2A*. **c**, Uptake of ^{59}Fe-ferrioxamine B is unaffected in *ΔISIP2A*, suggesting an alternate pathway for uptake of iron–siderophore complexes. **d**, Effect of a clathrin-mediated endocytosis (CME) inhibitor on short-term ^{59}Fe′ uptake rates, wild-type *P. tricornutum*. **e**, Upon addition of iron to iron-limited cells, the membrane-impermeable FM1-43 stain is internalized into vesicle-like inclusions. Scale bar, 5 μm. Pink is plastid auto-fluorescence. **b**, Data are mean ± s.e.m.; two-sided heteroscedastic *t*-test, *n* = biological replicates for wild-type and ISIP2A are indicated in brackets as (WT, ISIP2A) and *P* values are indicated. 12 pM Fe′ (5, 3), $P = 0.008$; 22 pM Fe′ (7, 5), $P = 0.003$; 43 pM Fe′ (6, 4), $P = 0.006$; 83 pM Fe′ (4, 4), $P = 0.007$; 165 pM Fe′ (3, 3), $P = 0.07$. **d**, Data are mean ± s.e.m.; $n = 3$ biological replicates; two-sided *t*-test, $P = 0.009$.

© 2018 Macmillan Publishers Limited, part of Springer Nature. All rights reserved.

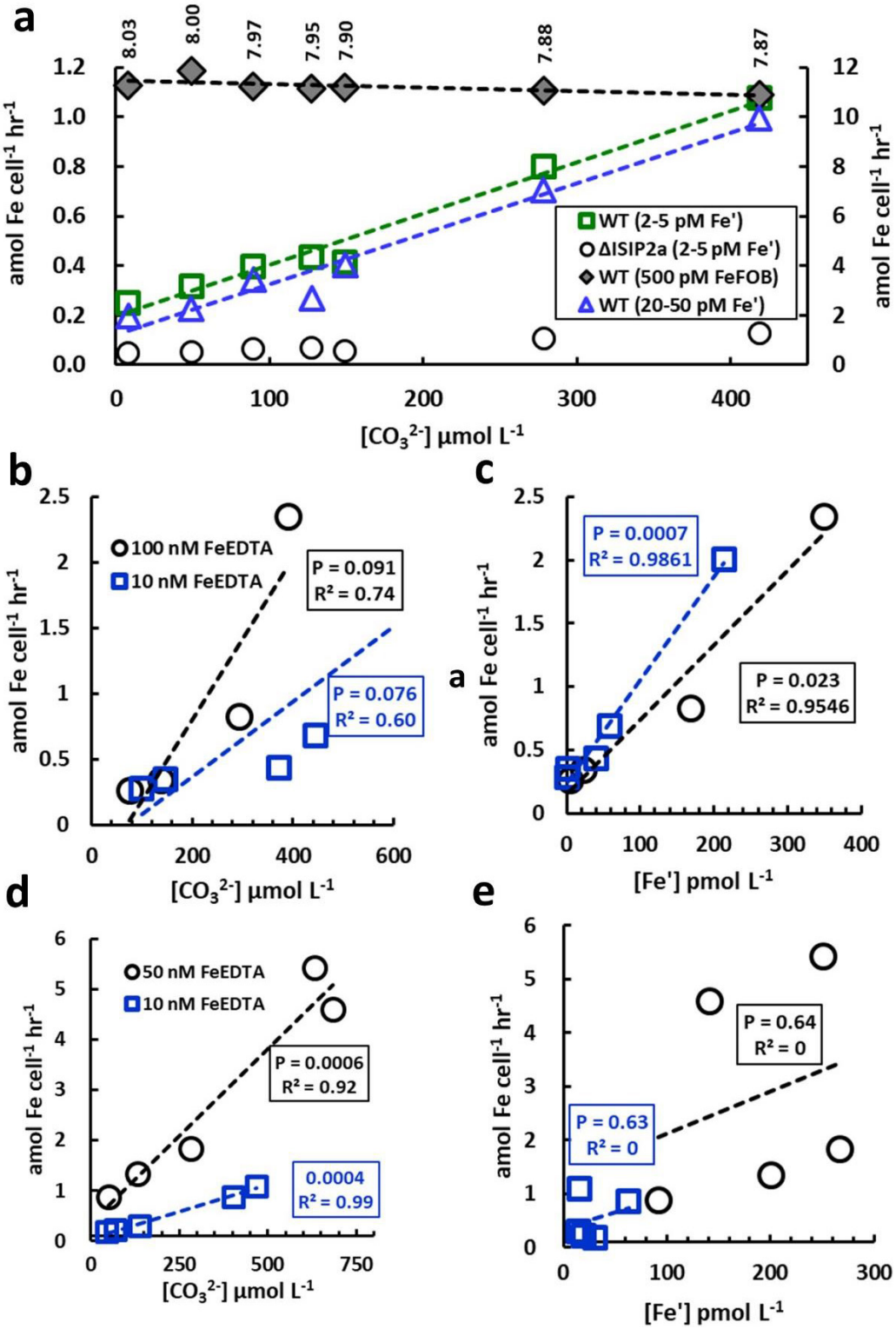

Extended Data Figure 5 | Reconciliation of the carbonate effect with the influence of acidification on seawater iron chemistry. a, Linearized representation of Fig. 3a, with high iron uptake rates (blue triangles) plotted on the secondary *y* axis, and pH values for each $[CO_3^{2-}]$ listed at top. Fe–FOB uptake rates decrease with pH, consistent with the findings of ref. 26, whereas Fe′ uptake rates increase with decreasing pH, inconsistent with the hypothesized effects of acidification on iron–EDTA chemistry[26]. This inconsistency is resolved when uptake rates are plotted as a function of the synergistic interaction between Fe′ and CO_3^{2-} (Fig. 3b). **b**, **c**, Under CO_2-induced acidification, the strong influence of pH on [Fe′] results in a significant correlation of uptake to [Fe′], although the interaction Fe′ and CO_3^{2-} results in a better fit (Fig. 4a, solid line). **d**, **e**, When the change in [Fe′] is constrained relative to pH and $[CO_3^{2-}]$, uptake rates are positively correlated with $[CO_3^{2-}]$ and uncorrelated to [Fe′], revealing the influence of the carbonate ion on Fe′ uptake rates. For statistical analyses of the linear regressions, see Extended Data Table 4.

© 2018 Macmillan Publishers Limited, part of Springer Nature. All rights reserved.

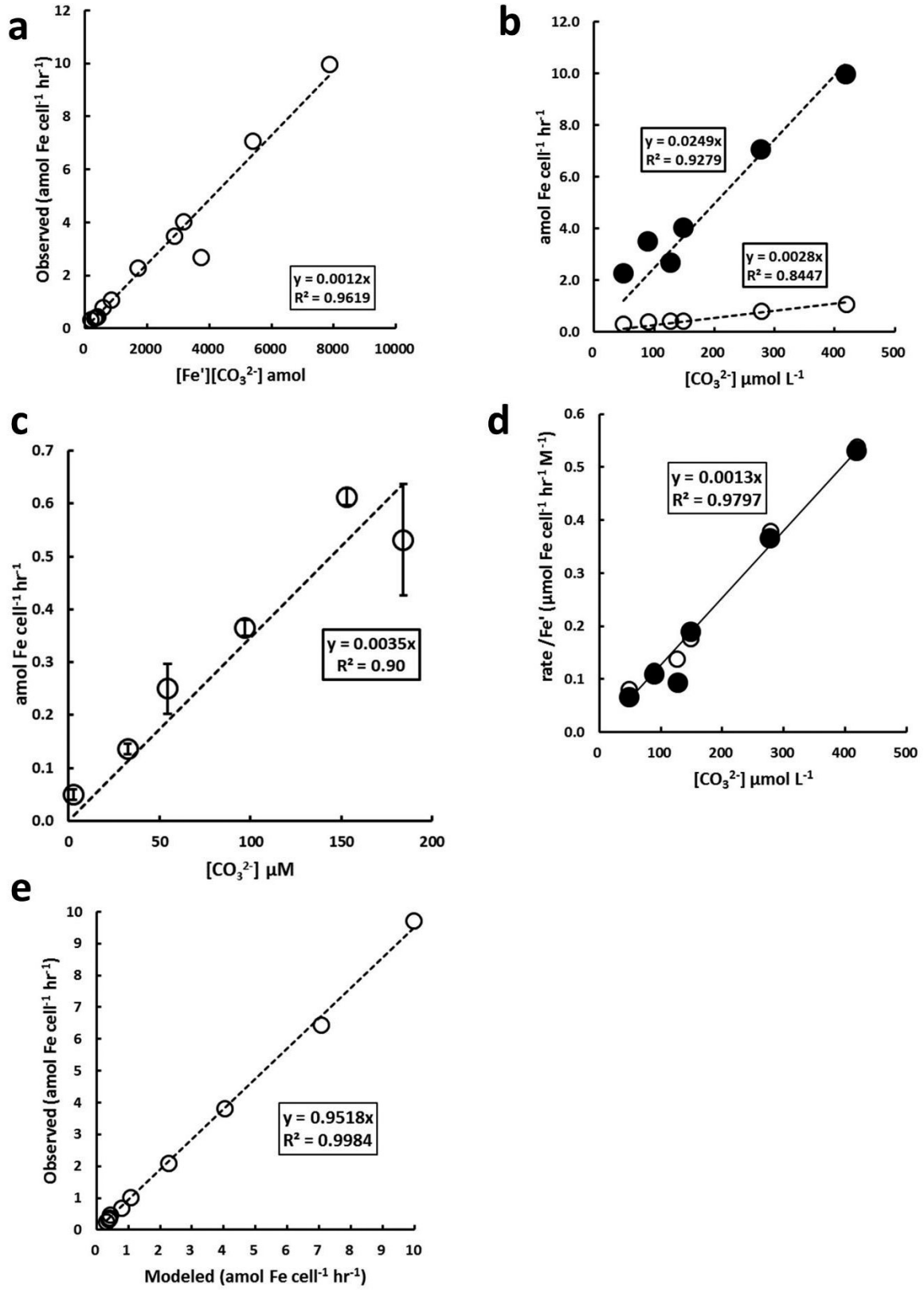

Extended Data Figure 6 | Derivation of second-order and constitutive rate constants from *P. tricornutum* resuspended in $NaHCO_3$-manipulated medium. a, Regression of the interaction product of Fe′ and CO_3^{2-}. Regression excludes the two observations in which the medium was not supplemented with $NaHCO_3$. **b**, ^{59}Fe uptake rates for treatments incubated with low (2–5 pM Fe′, open symbols) and high (20–50 pM Fe′, closed symbols) ^{59}Fe versus $[CO_3^{2-}]$. **c**, Demonstration of reproducibility at low [Fe′]. Data are mean ± s.e.m.; $n = 3$ biological replicates. **d**, Uptake rates normalized to [Fe′], plotted against $[CO_3^{2-}]$. The slope has units of mol Fe cell^{-1} h^{-1} (M Fe′)$^{-1}$ (M CO_3^{2-})$^{-1}$, equivalent to the pseudo-first-order uptake rate with respect to carbonate. **e**, Rates of uptake calculated as a function of [Fe′] and $[CO_3^{2-}]$ versus measured rates.

© 2018 Macmillan Publishers Limited, part of Springer Nature. All rights reserved.

Extended Data Table 1 | Uptake rates compared to the measured (in bold) and derived concentrations of Fe′ and carbonic acid species, in Aquil uptake medium

	Treatment	Fe' uptake amol Fe·cell^{-1}·hr^{-1}	[DIC] µmol kg^{-1}	[TA] µmol kg^{-1}	pH	[CO_3^{2-}] µmol L^{-1}	[Fe'] pmol L^{-1}	[Fe']x[CO_3^{2-}] fmol^2 L^{-2}	[EDTA] µmol L^{-1}	[Fe_{TOTAL}] nM	log K'$_{dark}$, 20°C
10 nM FeEDTA *P.tricornutum*	6 mM $NaHCO_3$	**1.076**	**5557**	-	**7.87**	419	2.0	0.84	100	10.8	-7.731
	4 mM $NaHCO_3$	**0.800**	**3647**	-	**7.88**	278	2.1	0.59	100	10.9	-7.716
	2 mM $NaHCO_3$	**0.412**	**1884**	-	**7.90**	149	2.3	0.35	100	11.0	-7.674
	1.5 mM $NaHCO_3$	**0.433**	**1437**	-	**7.95**	127	3.1	0.40	100	11.0	-7.545
	1 mM $NaHCO_3$	**0.396**	**970**	-	**7.97**	90	3.4	0.31	100	10.8	-7.499
	0.5 mM $NaHCO_3$	**0.318**	**505**	-	**8.00**	49	4.0	0.20	100	10.9	-7.436
	unamended	**0.250**	**75**	-	**8.03**	8	4.9	0.04	100	10.9	-7.347

	Treatment	Fe' uptake amol Fe·cell^{-1}·hr^{-1}	[DIC] µmol kg^{-1}	[TA] µmol kg^{-1}	pH	[CO_3^{2-}] µmol L^{-1}	[Fe'] pmol L^{-1}	[Fe']x[CO_3^{2-}] fmol^2 L^{-2}	[EDTA] µmol L^{-1}	[Fe_{TOTAL}] nM	log K'$_{dark}$, 20°C
100 nM FeEDTA *P.tricornutum*	6 mM $NaHCO_3$	**9.967**	**5557**	-	**7.87**	419	18.8	7.89	100	101.4	-7.731
	4 mM $NaHCO_3$	**7.071**	**3647**	-	**7.88**	278	19.4	5.42	100	101.1	-7.716
	2 mM $NaHCO_3$	**4.032**	**1884**	-	**7.90**	149	21.3	3.17	100	100.5	-7.674
	1.5 mM $NaHCO_3$	**2.694**	**1437**	-	**7.95**	127	29.1	3.71	100	102.0	-7.545
	1 mM $NaHCO_3$	**3.433**	**970**	-	**7.97**	90	32.1	2.88	100	101.2	-7.499
	0.5 mM $NaHCO_3$	**2.264**	**505**	-	**8.00**	49	34.7	1.71	100	94.7	-7.436
	unamended	**1.960**	**75**	-	**8.03**	8	45.2	0.36	100	100.4	-7.347

	Treatment	Fe' uptake amol Fe·cell^{-1}·hr^{-1}	[DIC] µmol kg^{-1}	[TA] µmol kg^{-1}	pH	[CO_3^{2-}] µmol L^{-1}	[Fe'] pmol L^{-1}	[Fe']x[CO_3^{2-}] fmol^2 L^{-2}	[EDTA] µmol L^{-1}	[Fe_{TOTAL}] nM	log K'$_{dark}$, 20°C
10 nM FeEDTA ΔISIP2a	6 mM $NaHCO_3$	**0.129**	**5557**	-	**7.87**	419	2.0	0.84	100	10.8	-7.731
	4 mM $NaHCO_3$	**0.107**	**3647**	-	**7.88**	278	2.1	0.59	100	10.9	-7.716
	2 mM $NaHCO_3$	**0.057**	**1884**	-	**7.90**	149	2.3	0.34	100	10.9	-7.674
	1.5 mM $NaHCO_3$	**0.070**	**1437**	-	**7.95**	127	3.1	0.40	100	10.9	-7.545
	1 mM $NaHCO_3$	**0.066**	**970**	-	**7.97**	90	3.5	0.31	100	11.0	-7.499
	0.5 mM $NaHCO_3$	**0.052**	**505**	-	**8.00**	49	4.0	0.20	100	10.9	-7.436
	unamended	**0.049**	**75**	-	**8.03**	8	4.9	0.04	100	10.9	-7.347

	Treatment	Fe' uptake amol Fe·cell^{-1}·hr^{-1}	[DIC] µmol kg^{-1}	[TA] µmol kg^{-1}	pH	[CO_3^{2-}] µmol L^{-1}	[FeFOB] pmol L^{-1}	[Fe']x[CO_3^{2-}] fmol^2 L^{-2}
500 pM FeFOB *P.tricornutum*	6 mM $NaHCO_3$	**1.090**	**5557**	-	**7.87**	419	500	-
	4 mM $NaHCO_3$	**1.106**	**3647**	-	**7.88**	278	500	-
	2 mM $NaHCO_3$	**1.117**	**1884**	-	**7.90**	149	500	-
	1.5 mM $NaHCO_3$	**1.116**	**1437**	-	**7.95**	127	500	-
	1 mM $NaHCO_3$	**1.123**	**970**	-	**7.97**	90	500	-
	0.5 mM $NaHCO_3$	**1.187**	**505**	-	**8.00**	49	500	-
	unamended	**1.126**	**75**	-	**8.03**	8	500	-

These data were used to generate Fig. 3a, b. Note, total alkalinity (TA) was not measured in any of these samples because 2 mM Tris-HCl was used to maintain the pH at approximately 8.0.

© 2018 Macmillan Publishers Limited, part of Springer Nature. All rights reserved.

Extended Data Table 2 | Uptake rates compared to measured (in bold) and derived concentrations for both Fe′ and carbonic acid species

		CO_2 (ppm)	Fe′ uptake amol cell^{-1} hr^{-1}	[DIC] µmol kg^{-1}	[TA] µmol kg^{-1}	pH	$[CO_3^{2-}]$ µmol L^{-1}	[Fe'] pmol L^{-1}	$[Fe']x[CO_3^{2-}]$ amol^2 L^{-2}	K'_{DARK}, 21.5°C	[EDTA] µmol L^{-1}	[Fe:EDTA] nmol L^{-1}
Nat. Seawater vs. Aquil (Fig. 3d)	Natural Seawater Ross Sea	200	**0.483**	**1837**	**2328**	8.36	320	21.1	6767	-6.550	100	7.5
		amb.	**0.064**	**2099**	**2324**	7.94	154	2.0	312	-7.570	100	7.5
		1000	**0.101**	**2045**	**2342**	8.07	199	4.2	832	-7.254	100	7.5
	Natural Seawater North Pac	200	**0.645**	**1874**	**2387**	8.38	337	23.6	7952	-6.502	100	7.5
		amb.	**0.175**	**2058**	**2371**	8.09	210	4.7	979	-7.206	100	7.5
		1000	**0.128**	**2091**	**2397**	8.07	206	4.2	860	-7.254	100	7.5
	Synthetic Seawater (Aquil)	200	**0.525**	**509**	**1012**	8.81	189	26.1	4943	-5.458	100	7.5
		amb.	**0.315**	**2070**	**2450**	8.18	255	7.7	1973	-6.987	100	7.5
		1000	**0.092**	**830**	**1047**	8.14	94	6.2	581	-7.084	100	7.5

	Fe′ uptake amol cell^{-1} hr^{-1}	[DIC] µmol kg^{-1}	[TA] µmol kg^{-1}	pH	$[CO_3^{2-}]$ µmol L^{-1}	[Fe'] pmol L^{-1}	$[Fe']x[CO_3^{2-}]$ amol^2 L^{-2}	K'_{DARK}, 21.5°C	[EDTA] µmol L^{-1}	[Fe:EDTA] nmol L^{-1}
Subs. Anions (Fig.3c)										
*Unamended	**0.049**	**27**	-	**8.059**	2.6	5.2	13.5	-7.282	100	7.5
*Carbonate	**0.263**	**1149**	-	**8.003**	97.2	3.8	278.5	-7.418	100	7.5
Formate	**0.052**	**27**	-	**8.063**	2.6	5.4	13.9	-7.271	100	7.5
Acetate	**0.090**	**41**	-	**8.051**	3.9	5.0	19.5	-7.299	100	7.5
Oxalate	**0.060**	**28**	-	**8.059**	2.8	5.2	14.8	-7.280	100	7.5
Glycolate	**0.097**	**20**	-	**8.067**	2.2	5.5	11.7	-7.263	100	7.5
Pyruvate	**0.099**	**36**	-	**8.019**	3.3	4.2	13.7	-7.377	100	7.5
$NaHCO_3$ (Fig. 6c)										
*Unamended	**0.049**	**27**	-	**8.059**	2.6	5.2	10.1	-7.282	100	7.5
0.5 mM $NaHCO_3$	**0.096**	**358**	-	**8.036**	32.6	4.6	112.7	-7.337	100	7.5
1.0 mM $NaHCO_3$	**0.170**	**603**	-	**8.036**	54.5	4.6	250.9	-7.336	100	7.5
*1.5 mM $NaHCO_3$	**0.263**	**1149**	-	**8.003**	97.2	3.8	278.5	-7.418	100	7.5
2.0 mM $NaHCO_3$	**0.318**	**1806**	-	**8.004**	153.1	3.8	441.4	-7.415	100	7.5
2.5 mM $NaHCO_3$	**0.420**	**2423**	-	**7.953**	184.1	2.9	398.9	-7.539	100	7.5

* duplicate data used in both experiments

Top, uptake rates of cells resuspended in two types of natural compared to synthetic seawater at ambient or modified with 200 and 1,000 p.p.m. CO_2. Uptake rates are an mean of three biological replicates. These data were used to generate Fig. 3d. Bottom, uptake rates of cells resuspended in synthetic seawater (Aquil medium) supplemented with 100 µM of carbonate or alternate synergistic anions, and data show the reproducibility of the $NaHCO_3$ manipulation experiment. All uptake rates are an average of three biological replicates. These data were used to generate Fig. 3c and Extended Data Fig. 6c, respectively.

© 2018 Macmillan Publishers Limited, part of Springer Nature. All rights reserved.

Extended Data Table 3 | Measured (in bold) and derived values for CO_2 and pH manipulation experiments

		CO_2 TREATMENT	Fe' uptake amol cell^{-1} hr^{-1}	[DIC] µmol kg^{-1}	[TA] µmol kg^{-1}	pH	$[CO_3^{2-}]$ µmol L^{-1}	[Fe'] pmol L^{-1}	$[Fe']x[CO_3^{2-}]$ amol^2 L^{-2}	[EDTA] µmol L^{-1}	$[Fe_{TOTAL}]$ nM	log K'$_{DARK}$, 20°C	µ	Fv/Fm
pH/CO_2 manipulations Δ[Fe']unconstrained	10 nM FeEDTA	50 ppm	**2.009**	**2052**	**2937**	8.66	605	214	129.3	100	14.4	-5.829	**1.21**	**0.606**
		200 ppm	**0.684**	**1903**	**2583**	8.52	444	58	25.7	100	8.5	-6.164	**1.02**	**0.613**
		400 ppm	**0.434**	**1802**	**2392**	8.45	373	40	14.9	100	8.4	-6.325	**1.13**	**0.577**
		1000 ppm	**0.349**	**2162**	**2391**	7.90	146	2	0.3	100	8.5	-7.664	**0.72**	**0.513**
		5000 ppm	**0.280**	**2488**	**2623**	7.67	100	0.8	0.1	100	14.2	-8.237	**0.48**	**0.431**
	100 nM FeEDTA	50 ppm	**7.358**	**1979**	**2891**	8.70	620	1831§	1135.3	100	100.0	-5.737	**1.14**	**0.587**
		200 ppm	**2.348**	**2000**	**2596**	8.40	391	350	136.5	100	100.9	-6.460	**1.22**	**0.605**
		400 ppm	**0.832**	**1989**	**2446**	8.27	292	168	49.0	100	97.5	-6.764	**1.29**	**0.611**
		1000 ppm	**0.345**	**2092**	**2311**	7.89	138	22	3.1	100	109.4	-7.691	**0.93**	**0.592**
		5000 ppm	**0.267**	**2288**	**2386**	7.58	76	3	0.3	100	97.5	-8.446	**0.70**	**0.504**

§The calculated concentration of Fe' exceeds the 750 pmol Fe' L^{-1} iron hydroxide precipitation limit, therefore this datapoint was not used in data models

		CO_2 TREATMENT	Fe' uptake amol cell^{-1} hr^{-1}	[DIC] µmol kg^{-1}	[TA] µmol kg^{-1}	pH	$[CO_3^{2-}]$ µmol L^{-1}	[Fe'] pmol L^{-1}	$[Fe']x[CO_3^{2-}]$ amol^2 L^{-2}	[EDTA] µmol L^{-1}	$[Fe_{TOTAL}]$ nM	log K'$_{DARK}$, 20°C	µ	Fv/Fm
pH/CO_2 manipulations Δ[Fe']constrained	10 nM FeEDTA	50 ppm	**1.089**	**1587**	**2335**	8.63	468	16	8.4	1000	12.0	-5.888	**1.05**	**0.584**
		200 ppm	**0.865**	**1803**	**2434**	8.47	403	63	25.5	100	12.1	-6.281	**1.11**	**0.598**
		400 ppm	**0.301**	**1874**	**2103**	7.92	138	14	1.9	20	12.0	-7.630	**1.02**	**0.578**
		1000 ppm	**0.221**	**2088**	**2183**	7.56	69	19	1.3	2	12.2	-8.499	**0.74**	**0.512**
		5000 ppm	**0.182**	**2900**	**2874**	7.23	46	30	1.4	0.2	11.7	-9.286	**0.77**	**0.517**
	50 nM FeEDTA	50 ppm	**4.605**	**1991**	**2987**	8.75	683	141	96.0	1000	55.2	-5.594	**1.12**	**0.603**
		200 ppm	**5.432**	**2315**	**3210**	8.61	631	250	157.8	250	55.2	-5.946	**1.23**	**0.617**
		400 ppm	**1.847**	**1632**	**2103**	8.33	282	267	75.4	50	55.1	-6.616	**1.06**	**0.581**
		1000 ppm	**1.348**	**1987**	**2201**	7.87	132	200	26.4	5	55.4	-7.744	**1.08**	**0.564**
		5000 ppm	**0.888**	**1918**	**1975**	7.44	49	91	4.5	1	55.4	-8.783	**0.92**	**0.541**

Top, CO_2 manipulations where the Fe:EDTA ratio was held constant, and Fe′ concentrations were allowed to change with changes in pH. Bottom, CO_2 manipulations in which the pH was allowed to change whereas the Fe:EDTA ratio was manipulated, constraining changes in [Fe′] to a narrow range (for full statistical analysis, see Extended Data Table 4).

© 2018 Macmillan Publishers Limited, part of Springer Nature. All rights reserved.

Extended Data Table 4 | Statistical analyses of $NaHCO_3$ and pH and CO_2 manipulations

Linear regression analysis, Fe' uptake

	FIGURE	Data set	term	DF	RSE	adj. R^2	F-stat	P-value	comment
$NaHCO_3$ manipulation (ΔpH constrained)	3a	WT Low Fe′	$[CO_3^{2-}]$	5	4.97×10^{-17}	0.972	212	2.76×10^{-5}	
	3a	WT High Fe′	$[CO_3^{2-}]$	5	6.13×10^{-16}	0.957	135	8.29×10^{-5}	
	3a	ΔISIP2a Low Fe′	$[CO_3^{2-}]$	5	8.54×10^{-18}	0.921	71	3.85×10^{-4}	
		WT Low Fe′	[Fe′]	5	1.86×10^{-16}	0.611	10	2.32×10^{-2}	
		WT High Fe′	[Fe′]	5	1.95×10^{-15}	0.565	9	3.13×10^{-2}	
		ΔISIP2a Low Fe′	[Fe′]	5	2.12×10^{-17}	0.514	7	4.23×10^{-2}	
	3b	WT (Combined Low/High)	$[Fe']x[CO_3^{2-}]$	12	5.96×10^{-16}	0.957	292	8.70×10^{-10}	
CO_2/pH manipulation (ΔFe' unconstrained)	Ext. 5b	WT Low Fe′	$[CO_3^{2-}]$	3	4.54×10^{-16}	0.601	7	7.68×10^{-2}	Not Significant
	Ext. 5b	WT High Fe′	$[CO_3^{2-}]$	2	4.92×10^{-16}	0.741	10	9.06×10^{-2}	Not Significant
	Ext.5c	WT Low Fe′	[Fe′]	3	9.81×10^{-17}	0.981	212	7.02×10^{-4}	
	Ext. 5c	WT High Fe′	[Fe′]	2	2.52×10^{-16}	0.932	42	2.30×10^{-2}	
	4a	WT (Combined Low/High)	$[Fe']x[CO_3^{2-}]$	7	9.13×10^{-17}	0.987	588	5.16×10^{-8}	Solid line
CO_2/pH manipulation (ΔFe' constrained)	Ext. 5d	WT Low Fe′	$[CO_3^{2-}]$	3	4.85×10^{-17}	0.987	292	4.36×10^{-4}	
	Ext. 5d	WT High Fe′	$[CO_3^{2-}]$	3	5.74×10^{-16}	0.922	48	6.15×10^{-4}	
	Ext. 5e	WT Low Fe′	[Fe′]	3	4.60×10^{-16}	0	0	6.34×10^{-1}	Not Significant
	Ext. 5e	WT High Fe′	[Fe′]	3	2.27×10^{-15}	0	0	6.47×10^{-1}	Not Significant
	4b	WT (Combined Low/High)	$[Fe']x[CO_3^{2-}]$	8	5.90×10^{-16}	0.898	80	1.93×10^{-5}	Dashed line

Significant interactions: 2-way Analysis of Variation (ANOVA), Fe' uptake

FIGURE	Experiment type	term	DF	Mean Sq	F	p-value
3b	$NaHCO_3$ manipulation (pH constrained)	[Fe′]	1	3.71×10^{-29}	131	4.55×10^{-7}
		$[CO_3^{2-}]$	1	4.13×10^{-29}	146	2.73×10^{-7}
		$[Fe']x[CO_3^{2-}]$	1	2.68×10^{-29}	95	2.02×10^{-6}
4a (Solid Line)	pH/CO_2 manipulation (Fe' unconstrained)	[Fe′]	1	4.53×10^{-30}	450	4.33×10^{-6}
		$[CO_3^{2-}]$	1	1.10×10^{-31}	11	$2.14\ 10^{-2}$
		$[Fe']x[CO_3^{2-}]$	1	2.63×10^{-31}	26	3.75×10^{-3}
4a (Dash Line)	pH/CO_2 manipulation (Fe' constrained)	[Fe′]	1	1.38×10^{-29}	43	5.89×10^{-4}
		$[CO_3^{2-}]$	1	1.22×10^{-29}	38	8.10×10^{-4}
		$[Fe']x[CO_3^{2-}]$	1	2.76×10^{-30}	9	2.58×10^{-2}

© 2018 Macmillan Publishers Limited, part of Springer Nature. All rights reserved.

nature research

Corresponding author(s): Andrew E. Allen

☐ Initial submission ☒ Revised version ☐ Final submission

Life Sciences Reporting Summary

Nature Research wishes to improve the reproducibility of the work that we publish. This form is intended for publication with all accepted life science papers and provides structure for consistency and transparency in reporting. Every life science submission will use this form; some list items might not apply to an individual manuscript, but all fields must be completed for clarity.

For further information on the points included in this form, see Reporting Life Sciences Research. For further information on Nature Research policies, including our data availability policy, see Authors & Referees and the Editorial Policy Checklist.

Experimental design

1. Sample size

Describe how sample size was determined.

No statistical methods were used to predetermine sample size. The sample sizes were determined , in part, based on availability of resources including time, cost, and personnel. All experiments for biochemical characterization of wild type and knockout cell lines and examination of the synergistic interaction of Fe' and carbonate on Fe' uptake rates were performed in biological triplicate This level of replication was determined sufficient to reliably discern statistical reproducibility and correlations with p-values below a 0.05 threshold.

2. Data exclusions

Describe any data exclusions.

One of the data points for the pH/pCO2 Fe' uptake curve exceeded Fe' solubility. As the Fe' concentration was unknown, this data point was not used in generating the curve. This omission is noted in the methods and in the supplementary data tables.

In determining the first order rate constants, samples unamended with bicarbonate were omitted from the analysis. This omission is noted in the figure legend.

3. Replication

Describe whether the experimental findings were reliably reproduced.

All experimental findings were reliably reproduced with sufficient biological replication.

4. Randomization

Describe how samples/organisms/participants were allocated into experimental groups.

All n numbers represent biological replicates, and the experiments were not randomized or blinded. There was no biased use of particular tubes or reagents that were correlated with experimental conditions. Care was taken to repeat experimental measurements in an unbiased way so as to mitigate the effect of cofactors such as sampling tubes, assay instrumentation, and reagents.

5. Blinding

Describe whether the investigators were blinded to group allocation during data collection and/or analysis.

Not applicable . Group allocation was not a feature for experiments and associated data.

Note: all studies involving animals and/or human research participants must disclose whether blinding and randomization were used.

6. Statistical parameters

For all figures and tables that use statistical methods, confirm that the following items are present in relevant figure legends (or in the Methods section if additional space is needed).

n/a	Confirmed
☐	☒ The exact sample size (*n*) for each experimental group/condition, given as a discrete number and unit of measurement (animals, litters, cultures, etc.)
☐	☒ A description of how samples were collected, noting whether measurements were taken from distinct samples or whether the same sample was measured repeatedly
☐	☒ A statement indicating how many times each experiment was replicated
☐	☒ The statistical test(s) used and whether they are one- or two-sided (note: only common tests should be described solely by name; more complex techniques should be described in the Methods section)
☐	☒ A description of any assumptions or corrections, such as an adjustment for multiple comparisons
☐	☒ The test results (e.g. *P* values) given as exact values whenever possible and with confidence intervals noted
☐	☒ A clear description of statistics including central tendency (e.g. median, mean) and variation (e.g. standard deviation, interquartile range)
☐	☒ Clearly defined error bars

See the web collection on statistics for biologists for further resources and guidance.

Software

Policy information about availability of computer code

7. Software

Describe the software used to analyze the data in this study.

CO2SYS was used for calculation of carbonate ion, dissolved inorganic carbon (DIC) concentration, and total alkalinity (TA) based on in situ temperature and salinity.

MAFFT was used for multiple sequence alignments.

PhyloBayes and RAxML 8.2.8 , BEAST 2, and SEAVIEW 4 were used for multiple sequence alignment and phylogentic analyses.

CLC software was used for molecular construct design.

Statistical analysis was performed in R.

For manuscripts utilizing custom algorithms or software that are central to the paper but not yet described in the published literature, software must be made available to editors and reviewers upon request. We strongly encourage code deposition in a community repository (e.g. GitHub). *Nature Methods* guidance for providing algorithms and software for publication provides further information on this topic.

Materials and reagents

Policy information about availability of materials

8. Materials availability

Indicate whether there are restrictions on availability of unique materials or if these materials are only available for distribution by a for-profit company.

No unique materials were used.

9. Antibodies

Describe the antibodies used and how they were validated for use in the system under study (i.e. assay and species).

Custom-made genomic antibodies targeting P. tricornutum ISIP2a, ISIP1, and β-carbonic anhydrase proteins were developed by the commercial vendor OriGene. Antibodies were validated using Western Blotting experiments examining P. tricornutum wild-type and knock-out cultures. All cell lines were genotyped to confirm KO alleles.

10. Eukaryotic cell lines

a. State the source of each eukaryotic cell line used.

P. tricornutum strain CCMP 632 was obtained from the National Center for Marine Algae and Microbiota. Transcription activator-like effector nucleases (TALENs) were used to disrupt the ISIP2a gene. Methods are described in the manuscript.

b. Describe the method of cell line authentication used.

Authentication for wild-type cells was confirmed by microscopy and by sequence verification of various alleles. (ISIP1, ISIP2a, ISIP3). Knockouts were confirmed by western blot using custom-made Genomic Antibodies (OriGene) targeting the ISIP2a protein.

c. Report whether the cell lines were tested for mycoplasma contamination.

The cell lines were confirmed to be free of heterotrphic bacterial contaminants, including Mycoplasma.

d. If any of the cell lines used are listed in the database of commonly misidentified cell lines maintained by ICLAC, provide a scientific rationale for their use.

No commonly misidentified cell lines were used.

Animals and human research participants

Policy information about studies involving animals; when reporting animal research, follow the ARRIVE guidelines

11. Description of research animals

Provide details on animals and/or animal-derived materials used in the study.

No animals were used in the study.

Policy information about studies involving human research participants

12. Description of human research participants

Describe the covariate-relevant population characteristics of the human research participants.

The study did not involve human research participants.